Assimilation of thermal emission spectrometer atmospheric data during the Mars Global Surveyor aerobraking period

Journal Item

Assimilation of Thermal Emission Spectrometer atmospheric data during the Mars Global Surveyor aerobraking period

Stephen R. Lewis, [a] Peter L. Read, [b] Barney J. Conrath [c]
John C. Pearl, Michael D. Smith [d]

[a] *Department of Physics & Astronomy, The Open University, Walton Hall, Milton Keynes MK7 6AA, UK.*

[b] *Atmospheric, Oceanic & Planetary Physics, Clarendon Laboratory, Parks Road, Oxford OX1 3PU, UK.*

[c] *Cornell University, Ithaca, NY 14853, USA.*

[d] *NASA Goddard Space Flight Center, Greenbelt, MD 20771, USA.*

Abstract

The Thermal Emission Spectrometer aboard the Mars Global Surveyor spacecraft has produced an extensive atmospheric data set, beginning during aerobraking and continuing throughout the extended scientific mapping phase. Temperature profiles for the atmosphere below about 40 km, surface temperatures and total dust and water ice opacities, can be retrieved from infrared spectra in nadir viewing mode. This paper describes assimilation of nadir retrievals from the spacecraft aerobraking period, $L_S = 190°$–$260°$, northern hemisphere autumn to winter, into a Mars general circulation model. The assimilation scheme is able to combine information from temperature and dust optical depth retrievals, making use of a model forecast containing information from the assimilation of earlier observations, to obtain a global, time-dependent analysis. Given sufficient temperature retrievals, the assimilation procedure indicates errors in the a priori dust distribution assumptions even when lacking dust observations; in this case there are relatively cold regions above the poles compared to a model which assumes a horizontally-uniform dust distribution. One major reason for using assimilation techniques is in order to investigate the transient wave behavior on Mars. Whilst the data from the 2-h spacecraft mapping orbit phase is much more suitable for assimilation, even the longer (45–24 h) period aerobraking orbit data contain useful information about the three-dimensional synoptic-scale martian circulation which the assimilation procedure can reconstruct in a consistent way. Assimilations from the period of the Noachis regional dust storm demonstrate that the combined assimilation of temperature and dust retrievals has a beneficial impact on the atmospheric analysis.

Key words: Mars, atmosphere; Atmospheres, dynamics; Meteorology

Icarus (2007), doi:10.1016/j.icarus.2007.08.009

1 Introduction

Data assimilation has been suggested by several authors (Banfield et al., 1995; Lewis and Read, 1995; Lewis et al., 1996, 1997; Houben, 1999; Kass, 1999) as an effective tool with which to analyze spacecraft observations of the martian atmosphere. The advantages of data assimilation for this problem are that it is able, in principle, to produce a consistent, four-dimensional mapping from a sparse, and possibly irregularly distributed, set of observations. Although only one or two atmospheric variables may typically be observed (e.g. temperature and dust opacity), a full, balanced analysis of all model variables will be produced (e.g. winds and surface pressure). Assimilation is also an ideal means by which to study transient, synoptic-scale atmospheric features, which may change significantly between successive observations of the same region by a single, orbiting spacecraft. This can lead to problems in global mapping. From another perspective, assimilation provides the most systematic means of testing and refining an atmospheric model against observations, and may also be used to produce realistic initial states for independent model studies and predictions. Finally, it is also possible to test the impact of different ensembles of observations to gain insight into which variables or patterns of observation would be most valuable in future missions or campaigns.

The loss of the Mars Observer and, subsequently, the Mars Climate Orbiter spacecraft has meant that the earlier studies mentioned above were restricted to trial assimilations, usually of model-generated data. There is now, however, a substantial atmospheric data set which has been accumulated from the Mars Global Surveyor (MGS) spacecraft and, in particular, the Thermal Emission Spectrometer (TES), which is able to supply information about surface temperatures, total dust and water ice opacities and atmospheric temperature profiles in the lower part of the atmosphere (Conrath et al., 2000; Smith et al., 2000).

Houben (1999) demonstrated an initial zonal-mean result, with TES data from near autumn equinox in the MGS aerobraking period, which uses a variational assimilation technique to strongly constrain a simplified atmospheric model. This provides a useful complementary analysis to that presented here, in which data is assimilated into a Mars general circulation model (MGCM) with full physical parameterizations using a sequential technique.

Kass (1999) also assimilated TES temperature profiles over a 25 sol, 17 orbit period during MGS aerobraking using Optimal Interpolation. He found that the winter hemisphere jet was moved polewards and that the amplitude

of waves became stronger compared to an independent experiment with the NASA Ames MGCM (Haberle et al., 1993).

Zhang et al. (2001) have published a study in which 10 sols of mapping phase temperature profile data from TES were assimilated, using techniques based on those presented by Banfield et al. (1995). Preliminary results from that study, for a relatively short period, were not entirely encouraging, since they suggested that it was crucial to specify an accurate background dust distribution for the model (dust information was not assimilated) and there also seemed to be little evidence that the assimilation was converging sufficiently well to capture the transient waves.

This paper discusses assimilations of retrievals of TES nadir profiles using a procedure based on the analysis correction scheme (Lorenc et al., 1991), a form of the successive corrections method which has proved simple and robust in trial studies with artificial data under martian conditions (Lewis and Read, 1995; Lewis et al., 1996, 1997). Some results have already been published which make use of the same technique and the much more extensive TES data set from the MGS mapping phase, which has now extended for about three Mars years, and has begun to be used in studies of atmospheric tides (Lewis and Barker, 2005) and dust storm variability (Montabone et al., 2005). The present paper describes an initial series of experiments conducted with TES observations made during the aerobraking phase of MGS, a time when the orbital period was being reduced from 45 to 24 h over the space of about 100 orbits. This configuration is far from optimal for assimilation, in particular because the period between orbits is significant compared both to the radiative timescale of 1–2 sols and the typical periods of transient waves of 2–10 sols (here "sol" is taken to mean a martian solar day, 88,775.2 s and times given in "hours" are taken to mean $1/24^{\text{th}}$ of a sol). Nonetheless, it forms an important test of the assimilation procedure in use with real data under challenging conditions. It also covers an interesting period of time from just after northern autumn equinox to nearly northern winter solstice (roughly areocentric longitudes, $L_S = 190°$–$260°$), a period of about 112 sols, which includes the regional Noachis dust storm at around $L_S = 225°$.

Sections 2 and 3 outline the model and assimilation scheme in use and Sec. 4 the TES retrievals which are assimilated and the quality control procedures applied. Results are described in Secs. 5–7, which respectively concentrate on the zonal-mean state of the atmosphere, some aspects of transient wave behavior in the assimilations and the assimilation of the Noachis dust storm. A summary and conclusions are presented in Sec. 8.

2 Mars General Circulation Model

The first requirement for data assimilation is a sufficiently realistic atmospheric model which will embody the appropriate physical constraints and be of high enough resolution to preserve useful information from the observations and represent any large-scale atmospheric phenomena which might be observed. The model used for this study is the semi-spectral (Oxford) version of the European MGCM, essentially as described by Forget et al. (1999). The model was run with a triangular spectral truncation at wavenumber 31 in the horizontal, with non-linear terms evaluated on a $3.75^\circ \times 3.75^\circ$ grid. In the vertical there were 25 levels covering the range 0–80 km, with three sponge levels above. The top of the model lies well above the altitude range covered by the nadir sounding retrievals, which extend to about 40 km. The region of the model atmosphere above that covered by data is able to respond to changes below and hopefully provides a realistic upper boundary condition. Wilson (1997) and Forget et al. (1999) demonstrated that a model with a top raised above at least 60 km is required to model the deep meridional circulation on Mars and to produce polar warmings. It is also of benefit to assimilate into a model which will be able to incorporate some limb-sounded profiles at a later date; these extend to above 60 km, but were not available for assimilation in the aerobraking period.

The main difference from Forget et al. (1999) was that the model here used the MOLA laser altimeter topographic data set (Smith et al., 1998) for both the resolved topographic map and the small-scale topographic parameters used for the gravity wave drag scheme. A new surface thermal inertia field was also employed, derived from TES data (Mellon et al., 2000) between 30°S and 60°N, blended with Viking observations from 60°S to 30°S (Palluconi and Kieffer, 1981) and in the polar regions (Paige et al., 1994; Paige and Keegan, 1994) where TES thermal inertia measurements were not available. The Viking thermal inertia values were uniformly reduced to match approximately the TES values in the regions of overlap, on the grounds that the effects of airborne dust were not properly accounted for in the original derivations (Haberle and Jakosky, 1991; Hayashi et al., 1995).

For a baseline, control integration, the model was run independently with a dust distribution which was constant both horizontally and in time, and which varied in the vertical according to

$$q = q_0 \exp\left[\nu \left(1 - p_0/p\right)\right] \tag{1}$$

for $p \leq p_0$, and $q = q_0$ for $p > p_0$, based on Conrath (1975), with $\nu = 0.01$ and $p_0 = 700$ Pa. q_0 was chosen to give a visible mean optical depth of $\tau = 0.36$ at $p = 610$ Pa. This opacity was chosen in the context of time- and latitudinal-

mean dust optical depths derived from TES retrievals, normalized to 610 Pa, and to give MGCM lower atmosphere and surface temperatures which were a reasonable match for the TES retrievals over the assimilation period. The assumption of dust which is constant in both time and latitude is clearly over-simplistic, as can be seen from observations (Smith et al., 2000). Moreover assimilation results shown later also imply that the dust loading increases with time over this period and that the poles are clearer than the equatorial regions, but this uniform initial distribution provides a useful reference simulation.

3 Data Assimilation Scheme

Data assimilation is conducted using a modified form of the analysis correction scheme (Lorenc et al., 1991), the parameters of which have been re-tuned for Mars firstly by scaling arguments and with various trial experiments using model data, described in (Lewis and Read, 1995; Lewis et al., 1996, 1997). The main features of the scheme, which is a form of successive corrections and is computationally inexpensive compared to the MGCM itself, are summarized here for reference.

The analysis correction scheme, in the configuration used for this study, involves a single analysis iteration between every dynamical time step of the model (480 times per sol at this resolution) which attempts to minimize, in a least-squares sense, the misfit between the model and the observations weighted by their relative errors. Continuous, repeated insertion of observations is conducted sequentially, assimilating each measurement at the time and place at which it is valid without prior interpolation. Observational increments to the model are spread in time and space by empirically-determined functions with scales which depend on the difference between the current model time and the time at which the data is valid.

Within each cycle of the assimilation scheme each model variable is analyzed in sequence (surface pressure, temperature, velocity and constituent measurements, e.g. dust and water vapor) followed by the derivation of multi-variate increment fields for dynamical balance. In the present case there is only an atmospheric temperature and a total dust opacity analysis at each horizontal grid point. Following the analysis of the temperature observations, increments to the model temperature field are balanced by non-divergent, thermal wind increments. This balancing procedure is conducted in order to avoid losing much of the newly introduced information to fast inertia-gravity waves (e.g. Daley, 1991). The spreading of observations in time by repeated insertion also favors the slower, meteorological modes.

The analysis correction scheme splits the analysis of increments into a vertical

step followed by a horizontal and temporal analysis. For temperature profiles, the vertical analysis is conducted by presenting the temperatures as mean values between a standard set of pressure boundaries, chosen to reflect the effective vertical resolution of the data, typically one pressure scale height in this case. The total model layer thickness calculated between these boundaries is adjusted to be consistent with the temperature retrievals, averaged between the same layer boundaries, with the intention that the vertical scale of the temperature increments should depend on the observational resolution rather than the model level spacing. This is important in order to prevent the assimilation disrupting small scale features, such as temperature inversions near the ground, which may be represented by the stretched model grid, but which may not be resolved in the remotely-sensed data. The layer thickness procedure is not an ideal solution to the problem. Another option is to assimilate radiances calculated from the model with the true instrument weighting functions, thus avoiding the need to use independent retrievals at all, but this is a significant enhancement in terms of complexity and sophistication which is planned for the future.

The horizontal analysis is conducted by calculating increments to the model variables on the model grid, Δx_k, from increments at the observation locations, C_i, using

$$\Delta x_k = \lambda \sum_i \mu_{ki} \tilde{Q}_i R_i^2(\delta t_i) C_i \tag{2}$$

where the index k refers to a model grid point and the index i to an observation. The normalization factor, $\tilde{Q}_i$, is a function of the ratio of observational to first guess error and of the local observation density around each observation location (Lorenc et al., 1991). For simplicity, the relative error of each observation is here taken to be equal since they are all of the same type, although more detailed error information could be incorporated.

Observational increments are spread in time by the function $R(\delta t)$, where δt is the time difference between the current model and observation time, see Fig. 1. The function first acquires observations 5 h before they are valid and finally discards them 1 h after their valid time. The asymmetry in time of the function is ideal for the problem of the assimilation of observations from a single satellite since it biases the assimilation gains toward the direction of motion of the satellite ground track, which is generally a region of the atmosphere which has not been observed recently. Spreading in time was also found to be beneficial in the case of relatively sparse data, where it is often better to use an observation from a slightly different time, with a reduced weight, rather than release the model which would then quickly relax back toward a temperature determined principally by its dust distribution, since the radiative timescale of the martian atmosphere is only 1–2 sols.

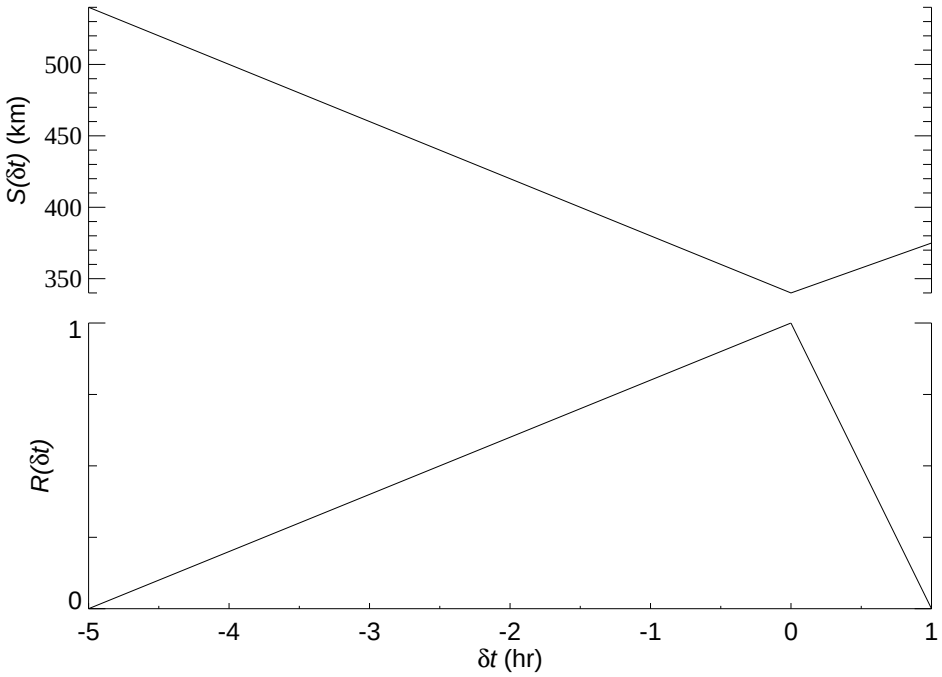

Fig. 1. Lewis et al. Assimilation of atmospheric data during MGS aerobraking

In the horizontal, the observational increments are spread by a second-order auto-regressive function of the distance, r_{ki}, between the observation and each model grid point

$$\mu_{ki} = (1 + r_{ki}/S_i(\delta t_i)) \exp(-r_{ki}/S_i(\delta t_i)) \tag{3}$$

where the correlation scale of the function, $S(\delta t)$, is a function of δt, such that $S(\delta t)$ is large at $\delta t = -5$ hr, falls to a minimum at $\delta t = 0$ hr and increases again until the observations are discarded at $\delta t = +1$ hr, see Fig. 1. Thus increments from observations with a low weight at the start of their insertion period are given a large scale which becomes more focused as their valid time approaches and their weight increases.

The forms of $R(\delta t)$ and $S(\delta t)$ are guided by extensive terrestrial experience (Lorenc et al., 1991) and the length and time scales have been previously tuned in twin Mars model experiments (Lewis et al., 1996, 1997, e.g.), which indicate that the assimilation scheme is not highly sensitive to these parameters over a reasonable range. The length and time scales used for the present study were varied by a factor of two in each direction, but variations in each direction degraded the assimilation compared to the parameters shown in Fig. 1.

The parameter λ in Eq. 2 determines the fraction of the analyzed increment that is added onto the model field. It can be related to a "nudging coefficient"

(Davies and Turner, 1977), G, by

$$G = \lambda/(1-\lambda)\Delta t \tag{4}$$

if the model dynamical time step is Δt and the analysis correction process is regarded as equivalent to adding an implicit relaxation term $G(\mathbf{x}_{\rm obs}-\mathbf{x})$ to the right hand side of the model equation for $\mathbf{x}$, with $\mathbf{x}_{\rm obs}$ the analyzed observation of $\mathbf{x}$. The best results in test cases were found when G was set at a value of 5×10^{-4} s^{-1}, with a linear reduction, between 30° and 20° latitude in both hemispheres, to an equatorial value of 4×10^{-4} s^{-1}. Reduced assimilation increments at the equator were found to make a small improvement in the degree of convergence, compared to the trial results shown in Lewis et al. (1996), and are justified since the efficiency of the assimilation is governed by the ratio of the timescale G^{-1} to the rotational timescale f^{-1} (Lorenc et al., 1991; Lyne, 1979).

For an observation-model temperature misfit of 4 K, and assuming an extra-tropical location, the assimilation scheme would produce a peak forcing rate at the precise observation location and time of 2×10^{-3} K s^{-1}, or a peak increment of 0.4 K over one assimilation iteration (run 480 times per sol). With the $R^2(\delta t)$ factor in Eq. 2, the total increment is almost 30 K integrated over the full 6-h time window, with half of that applied in the hour before, and the fifth of an hour following, the time at which the observation is valid. These estimates have been made with the assumption that the model acts against the assimilation increments to maintain a steady disagreement with the observations. Left to itself, the assimilation scheme will tend to bring model and observations into agreement on an e-folding time of 0.5 hr, close to the valid time, reducing the total increments. As a result of the horizontal spreading of increments, Eq. 3, a similar increment will be applied to temperatures in the surrounding area, falling by a factor of a half over a horizontal radius of around 570 km, or about 3 model grid points. The horizontal region of influence for each observation is cut off at $3.5S(\delta t)$, or about 1200 km.

Geostrophic balance increments to the winds, based on assimilated temperature increments, are re-scaled by a factor of 0.7 in the extra-tropics, poleward of 30° latitude, with the factor reducing to zero within 20° of the equator. The vertical scaling for geostrophic wind increments was further simplified so that the full increment is applied as far as the model top, rather than decreasing at high altitudes (Lewis et al., 1997); again this was found to make some small improvements in test assimilations.

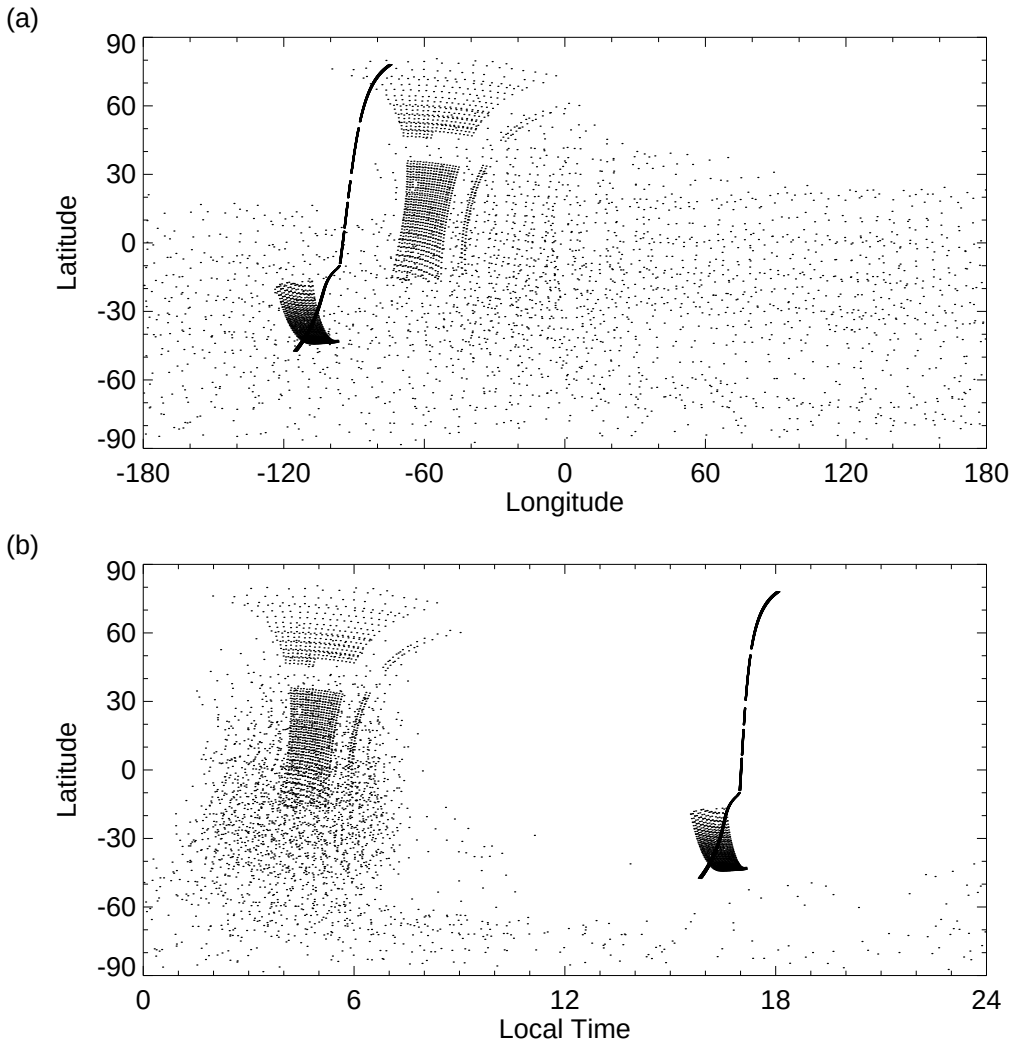

Fig. 2. Lewis et al. Assimilation of atmospheric data during MGS aerobraking

4 Thermal Emission Spectrometer Data

The atmospheric retrievals from TES observations which are used for these assimilations are described in more detail by Conrath et al. (2000) and Smith et al. (2000). The revised version 2 (NASA Planetary Data System) atmospheric retrievals from nadir soundings for MGS orbits 3–100 are used here, as are retrievals of total dust optical depth. TES measurements of surface temperature, solar illumination, water vapor or seasonal polar cap edge were not used in the present assimilation. During this time the orbital period of MGS was reduced from 45 to about 24 h and the spacecraft was in a highly elliptical orbit. This results in a data set which is irregular in distribution in both time and space, typically with relatively few observations in northern high latitudes. There is a densely-sampled stripe of observations, made as the spacecraft flew low close to perihelion, generally in late afternoon local time,

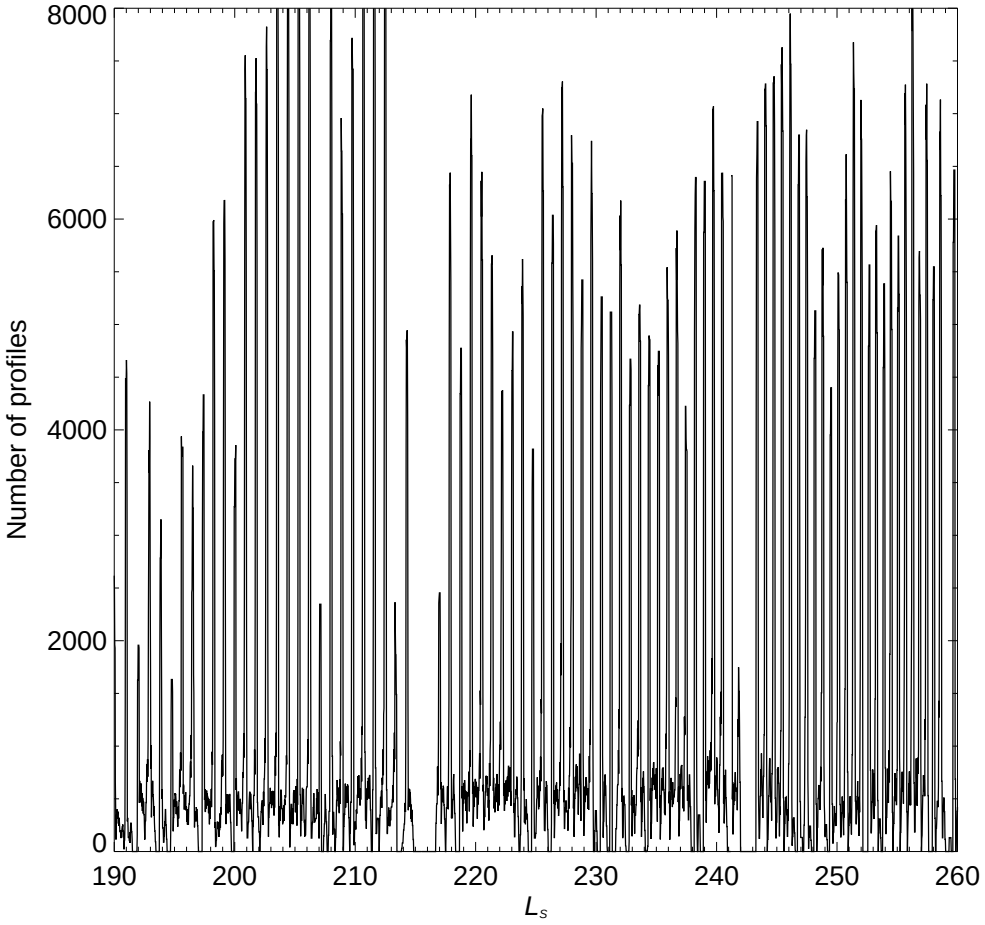

Fig. 3. Lewis et al. Assimilation of atmospheric data during MGS aerobraking

and a more disperse set from around aphelion, generally on the night-side of Mars. This is illustrated for all the available retrievals from MGS orbit 26 in Fig. 2 as a function of both latitude–longitude and latitude–local time of day. It should be noted that this orbit is not typical, but is one which provided a larger number of observations and better coverage than average (a total of 10,518 temperature profiles compared to an average of 6,740 per orbit over orbits 3–100).

During aerobraking the observation footprint varies from around 1 km at periapsis (with at least 10 km along-track smearing) to around 340 km at apoapsis (apoapsis was at 41,500 km for MGS orbit 50), based on the 8.3 mrad wide TES pixel. The assimilation scheme spreads increments over a horizontal region always larger than the size of the footprint, with a minimum value of $S(0) = 340$ km in Eq. 3.

Fig. 3 shows the total number of temperature profiles which fall within a sliding six-h window, and so would be used by the assimilation scheme, throughout the aerobraking assimilation period. It is apparent that there are irregular peaks of observations from some orbits, while at other times during the period there are few, if any, observations available. For example, there is a complete break in the observational record at $L_S = 215°$ (orbit 39 provides no observations and orbit 40 very few), which lasts for more than 3 sols, longer than the martian radiative timescale (1–2 sols). Even at times of more regular coverage, the length of the orbital period over which coverage is sparse is still significant and poses a severe test of the assimilation procedure. In contrast, during the subsequent scientific mapping phase roughly 7,500 profiles fall within a six-h window for most of the time when the TES instrument is fully operational.

4.1 Data Post-Processing and Quality Control

The TES nadir temperature retrievals were provided on a one quarter pressure scale height (roughly 2.5 km) vertical grid. This is higher resolution than the instrument can effectively achieve in nadir sounding mode. The nadir weighting functions (Conrath et al., 2000), have a typical width of 10–15 km and nearly all the information comes from below 40 km altitude. To assimilate the profiles as presented directly would impose artificial smoothness on the model, especially near the surface. The temperature profiles were therefore re-sampled by averaging between five standard pressure levels (1658 Pa, 610 Pa, 224 Pa, 83 Pa, 30 Pa, 11 Pa), spaced at 10 km intervals in log-pressure height (-10–+40 km), to provide layer thicknesses which could be assimilated as discussed in Sec. 3 above. Where more than one half of an interval was not covered by the retrieved profile it was marked as missing data. This is usually the case for the lowest interval, included only for a few profiles over low terrain, but many profiles end well below 40 km, so the upper layer thickness is frequently absent as well.

The assimilation procedure should itself be able to filter out random errors and quality control for the temperature profiles was therefore kept to a minimum before presenting them to the scheme. Only nadir profiles marked as bad by the retrieval algorithm were rejected immediately. Even amongst the profiles marked as good retrievals, there were still a few questionable temperatures which caused intermittent problems to the model physical schemes. A further filter was implemented which rejected any temperature profiles which fell below 130 K (the condensation temperature for carbon dioxide is 145 K at typical martian surface pressures) or exceeded a limit of 300 K in the lower atmosphere (the upper limit falling linearly to 220 K at 40 km altitude). This filter only removed a few profiles, 3,700 or about 0.5 per cent of the total, which were re-checked and which indeed appeared unphysical. The vast majority of

temperature profiles were then available for assimilation.

The TES total dust opacities (Smith et al., 2000) had to be processed more carefully before assimilation. For nadir soundings, only a single dust opacity is retrieved, a fit to the total atmospheric opacity at 1075 cm^{-1}. Firstly, only retrievals marked as good quality for opacity values were considered, a much smaller set than the total number of temperature retrievals. Following Smith et al. (2000), only opacities where the surface temperature was greater than 220 K were then retained. This requirement, for a good surface–atmosphere temperature contrast, unfortunately further restricts the dust information to day-time, and mostly to the summer hemisphere, regions of the planet. Most dust information is in the equatorial region and the southern hemisphere. Finally, checks were run to see that the dust opacity was indeed positive, that the retrieved water ice opacity was also positive (actually $\tau > -0.05$, to allow for noise but to disallow fits which balanced large dust opacities with negative water ice opacities) and similarly to check that the carbon dioxide hot bands opacity fit was reasonable ($-0.01 > \tau < 0.05$) and that the total fit residual was not too large ($\tau < 0.05$). This quality control procedure resulted in about one third as many dust observations (239,155) as temperature profiles (660,741) being assimilated over the whole period. The total opacity was converted from the infrared wavelength (1075 cm^{-1}) where it was measured to a mean visible opacity suitable for the MGCM radiation scheme by multiplying by 2.0 (Clancy et al., 1995), although there is some uncertainty in the size of this factor (Martin, 1986). The retrieved opacities were also converted to opacity at a reference pressure of 610 Pa, using the same surface pressure as was assumed for the retrieval at each point.

Despite the quality control procedure, the dust observations which remain still appear somewhat noisy, and it was found to be beneficial to assimilate them with a lower weight; the error variance on observations was empirically assigned to be five times greater than that on the a priori model state, which is based on the assimilation of many past observations. Smith et al. (2000) estimate an uncertainty of 0.05 in the individual infrared opacities, translating to at least 0.1 in the visible opacities used here, which is significant on a typical total opacity of 0.4.

A further difficulty with the dust assimilation is that only a total column opacity is available, with no information on the vertical distribution. Clearly some information on the full three-dimensional distribution of dust would be highly desirable, and may be available in future with limb soundings. For the present study the choice was made to maintain a constant vertical profile, Eq. 1, and to assimilate the value q_0 to match the total visible opacity at 610 Pa to the normalized observations. There may be a case for lowering the top of the dust when the total amount becomes small, but this can become arbitrary in the absence of more detailed observations. In the present case,

the MGCM was not used to transport dust actively (Newman et al., 2002a), partly because of the difficulties in adjusting a three-dimensional field with two-dimensional information, but this remains an option in future work. By updating the MGCM dust field with two-dimensional variations, the present work is still a significant advance on earlier trial assimilations and model studies with uniform dust fields.

5 Global Circulation

Assimilation experiments were begun from an initial state at $L_S = 189.7°$, which had been generated from a multi-annual independent model integration under the constant dust conditions described in Sec. 2. In order to generate a small ensemble of plausible initial conditions, atmospheric fields were taken at several intervals around the principal initialization point and were then used as alternative initial conditions, and a set of similar integrations were performed with the amount of dust in the independent model experiment, and used as the starting point before TES assimilation, increased and decreased by 10 per cent in each case. The assimilations were each performed for a total of 112 sols, out to $L_S = 260.7°$, at which point no more nadir soundings were available for assimilation.

This section describes the effects of the assimilation on the global circulation. The large-scale, zonal-mean circulation in the assimilations was found to be largely insensitive to the choice of initial conditions after around 10 sols of assimilation. The zonal-mean fields shown in Figs. 4–9 were all taken from a single assimilation, but these are representative of the ensemble of assimilations which were conducted, including those begun with varying dust loading. A comparison of the zonal-mean, time-mean temperatures over each period found differences of up to 0.1 K below 40 km altitude and 0.3 K above. Correspondingly, the zonal-mean winds varied by up to 0.3 $\mathrm{m\,s^{-1}}$ below 40 km and 1.0 $\mathrm{m\,s^{-1}}$ above.

The first period under consideration is an average taken from the start of the assimilation, $L_S = 190°$–$200°$, a period which closely follows northern autumn equinox at $L_S = 180°$. Fig. 4 shows the assimilated zonal-mean temperature and zonal wind, averaged over this initial period. It should be noted that the observations are of temperature and none extend above about 40 km in log-pressure height. Changes in the temperature field above this height, and to the wind field, are produced by the model in response to the changes in the lower atmosphere. In this case, the lower atmosphere temperature is very similar to that shown by Conrath et al. (2000) for the same period, made by averaging the TES retrievals directly. In contrast, the zonal means shown here are true zonal means over all longitudes and local times of day and extend to regions

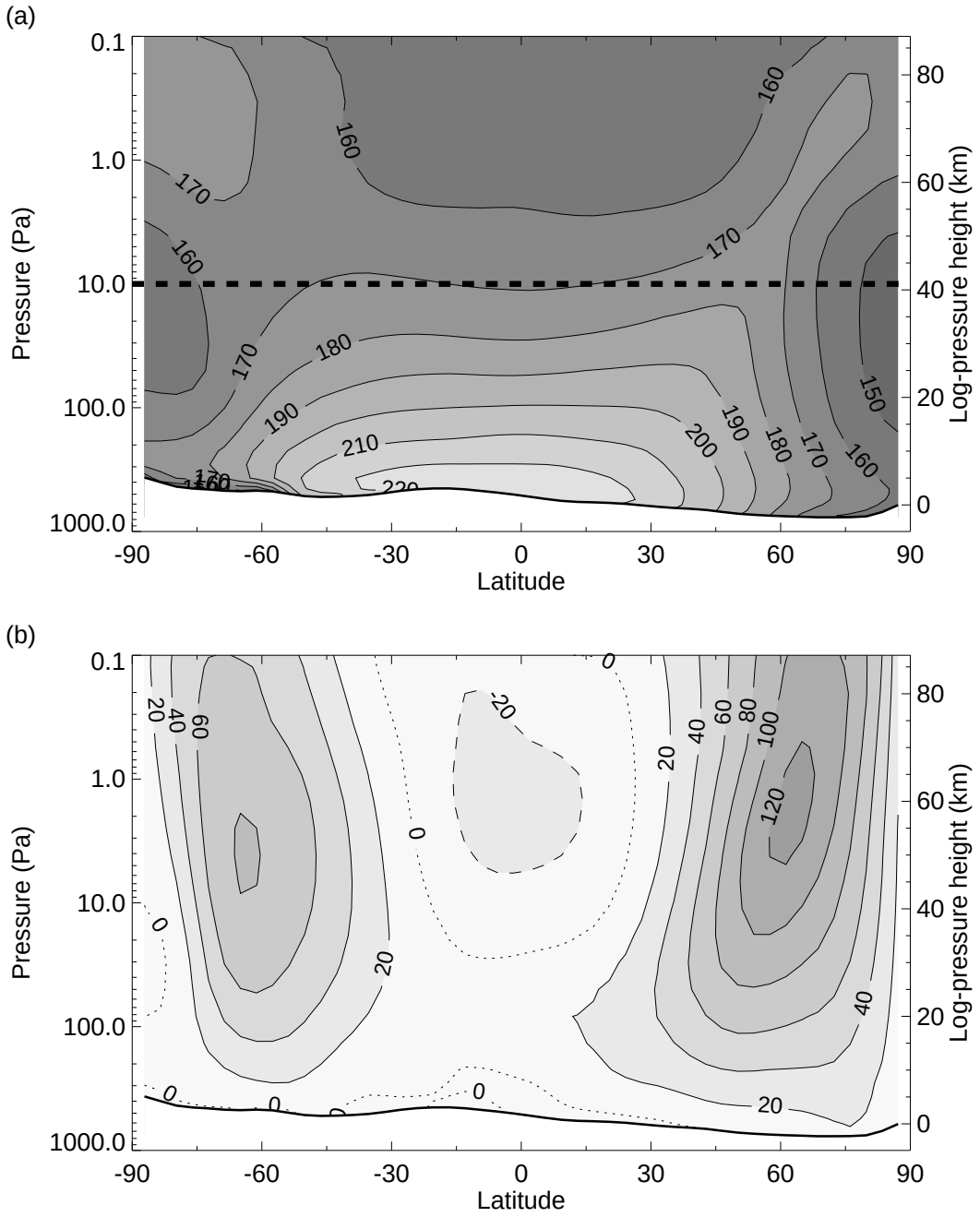

Fig. 4. Lewis et al. Assimilation of atmospheric data during MGS aerobraking

where TES made no observations. One noticeable difference is the small scale temperature inversion over the remnants of the southern polar cap, poleward of about 50°S, and to a lesser extent an inversion in northern polar regions. Neither is prominent in the retrievals, being of small vertical scale and close to the surface.

The zonal winds, shown in Fig. 4b, should be an improvement on the typical thermal or gradient wind balance winds which can be derived from a

zonal-mean temperature section, since they are effectively the result of a full primitive equations balance on the sphere and make no assumption of a level of no motion. At this time of year they do appear very similar to the gradient wind balance winds which could be derived, as shown by Conrath et al. (2000), with some indication of surface westerlies slightly increasing the magnitudes of the mid-latitude westerly jets, especially in the northern hemisphere, but otherwise zonal-mean surface wind speeds are low. There is notable evidence of retrograde flow high over the equator, and weak prograde, westerly flow above the equator between 5–30 km, indicating local super-rotation (Lewis and Read, 2003).

Fig. 5 shows the differences in zonal-mean fields between the assimilation shown in Fig. 4 and the control experiment with best-guess uniform dust. Lower atmosphere temperatures, Fig. 5a, especially near the equator, are actually very similar, largely because the total dust amount in the control run was adjusted to arrange this in order to provide a reasonable test for comparison against the assimilations. A small cooling in the 20–40 km region is evidence of the slightly increased vertical temperature gradient in the lower atmosphere of the assimilation. There is also evidence of an increase in the horizontal temperature gradient at 10–20 km around 60°N. Most striking here is the strong cooling (≈ 20 K) above the south pole. This is most likely an indication that there is much less dust in this region in reality than the assumption of horizontal uniformity on pressure surfaces in the control experiment. Indeed there is direct observational evidence for a clearer south pole (Smith et al., 2000). Finally, there is some evidence of an increased warming high above the north pole, in a region with no observations which is responding to changes in the mean meridional circulation driven from observations lower down and nearer to the equator.

The changes in zonal wind, Fig. 5(b), reflect the modifications to the zonal mean temperature gradients. There is a pattern showing a strengthening and narrowing of the westerly jet at 60°N below 60 km. The large changes to the south polar temperatures are associated with a significantly stronger westerly jet in the southern hemisphere, with enhanced horizontal wind shear around 75°S. High above the equator, the assimilation has a weaker easterly flow than is seen in the control experiment.

Figs. 6 and 7 are similar diagrams for the period $L_S = 225°$–$233°$, which covers the main part of the Noachis dust storm, a regional storm which began around 30°S at $L_S = 225°$. Compared to the $L_S = 190°$–$200°$ period, the atmosphere has moved toward a northern winter solsticial state with a strong equatorward horizontal temperature gradient and a powerful westerly jet of over 160 $\mathrm{m\,s^{-1}}$ at 60°N. Fig. 7a clearly illustrates the global rise in atmospheric temperatures in the lower and middle atmosphere, with a small cooling effect in the lowest 10 km, compared to the control simulation, which has no dust

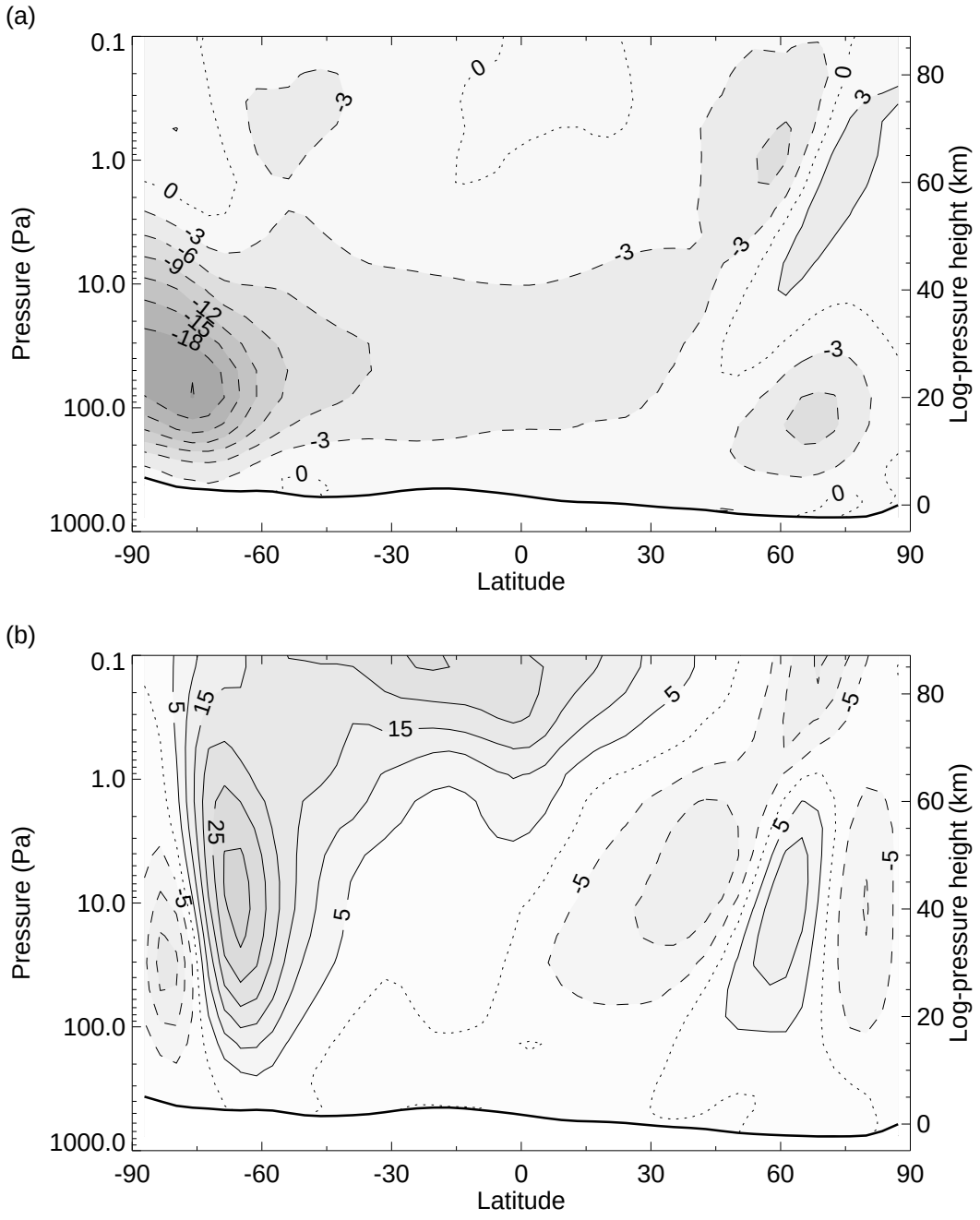

Fig. 5. Lewis et al. Assimilation of atmospheric data during MGS aerobraking

storm. The response of the upper atmosphere, where there are no measurements, is also evident as a cooling in high equatorial and southern hemisphere regions, together with a striking polar warming over the north pole, which is more than 15 K warmer than the control. This is a direct consequence of the enhanced cross-equatorial meridional circulation during this time, as described further in Sec. 7. Fig. 7(b) indicates that the northern hemisphere westerly jet is again strengthened and narrowed in the assimilation, though at lower altitudes (mainly below 20 km), compared to Fig. 5(b). The posi-

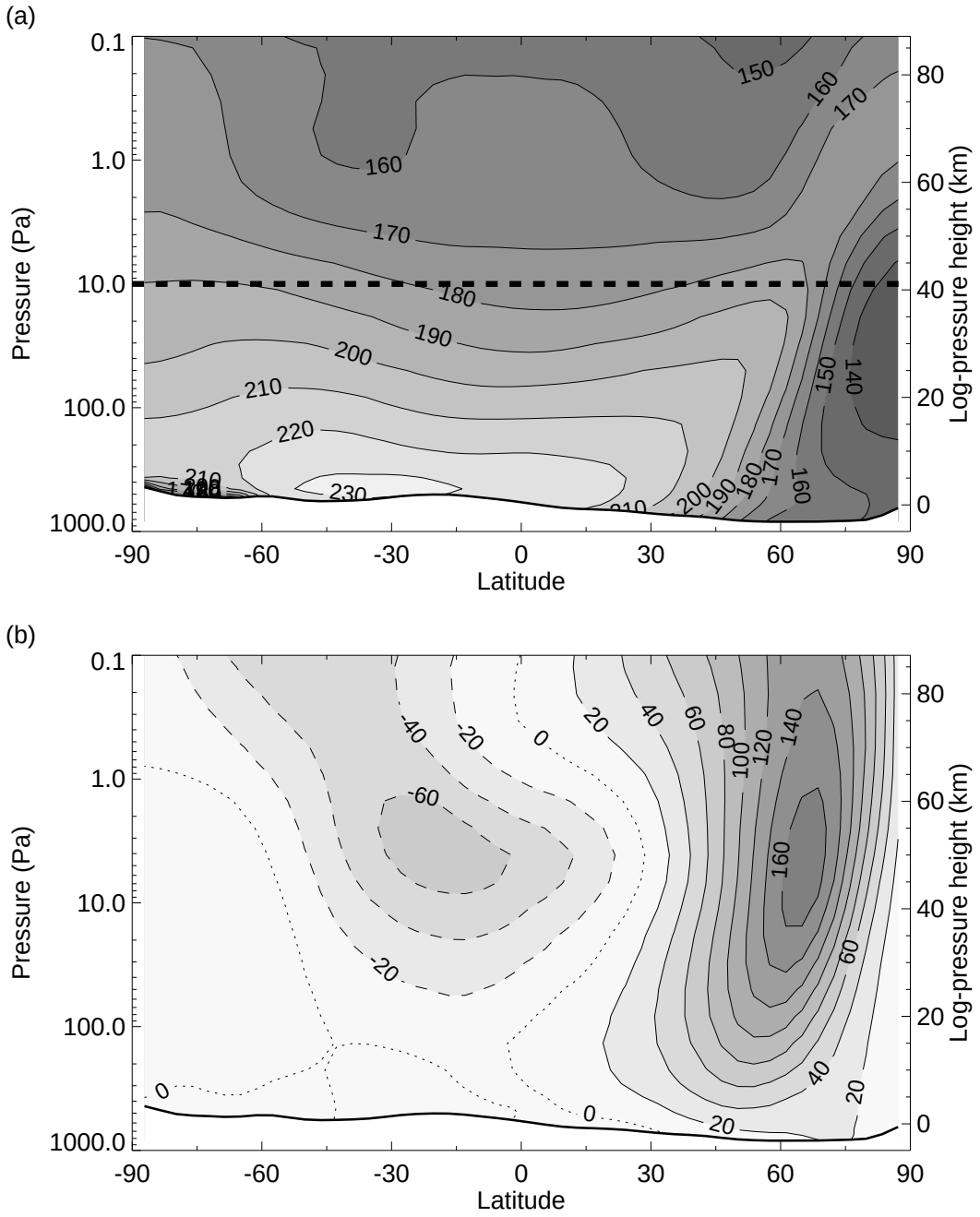

Fig. 6. Lewis et al. Assimilation of atmospheric data during MGS aerobraking

tive wind difference at high southern latitudes is actually a reflection of the low zonal winds in this region in the assimilation, Fig. 4(b), compared with an easterly flow in the control experiment. Above the equator the differences between the assimilation and control are driven by the changes in vertically propagating thermal tides, in particular the diurnal tide, which is stronger in the dustier assimilation and which leads to the enhanced westerly flow and super-rotation visible around 10 km altitude directly over the equator (Lewis and Read, 2003).

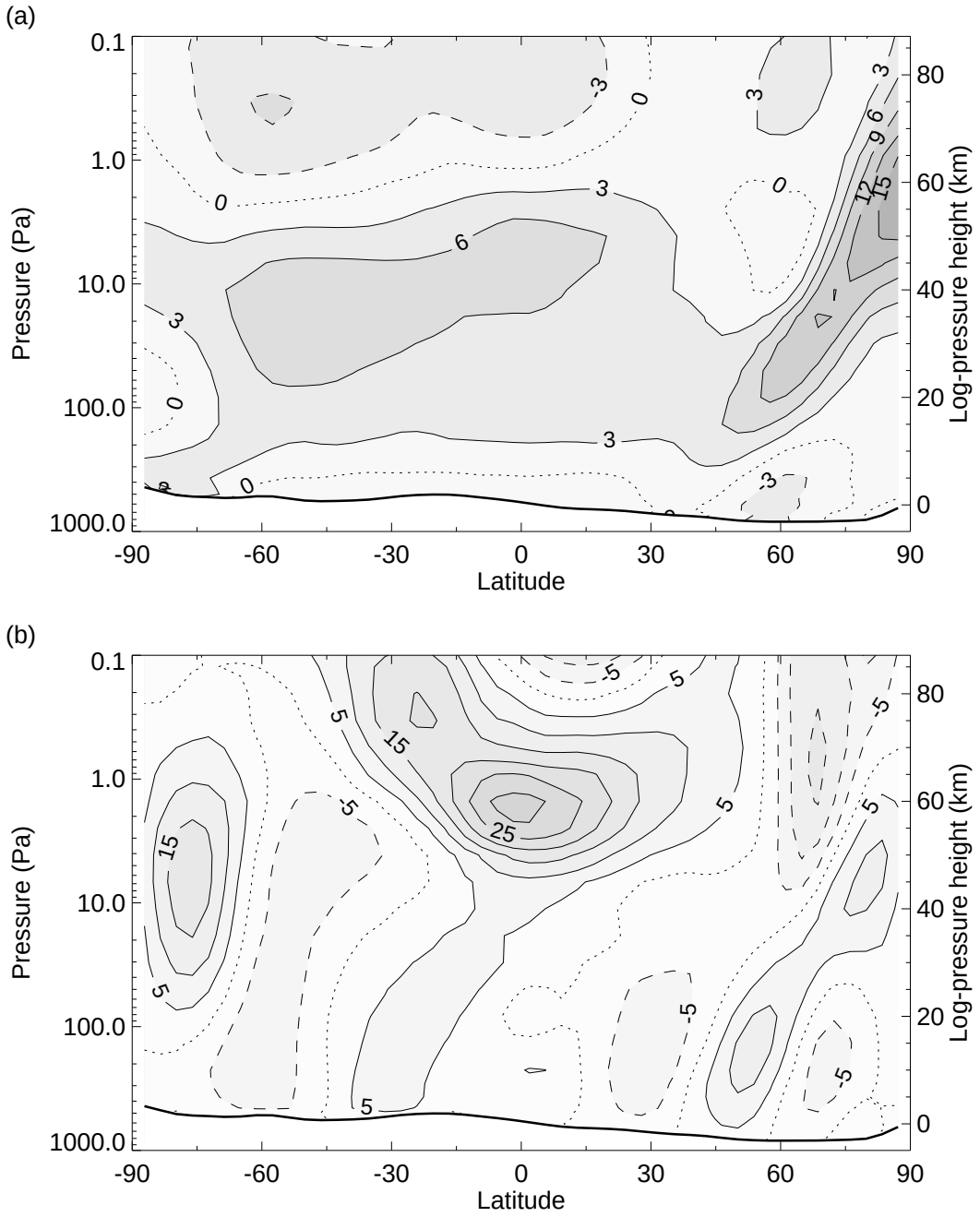

Fig. 7. Lewis et al. Assimilation of atmospheric data during MGS aerobraking

The final set of zonal-mean plots, Figs. 8 and 9, show the atmospheric state from $L_S = 250°$–$260°$, just before northern winter solstice ($L_S = 270°$) and after the main part of the Noachis dust storm had died away. High temperatures in the southern (summer) hemisphere are notable, Fig. 8a, except for a small region of inversion over the residual polar cap. The middle atmosphere is still warmer than the control experiment, Fig. 9a, indicating that dust levels remain higher than they were initially after the Noachis storm. Above the south pole, however, the assimilation is once again becoming cooler than the

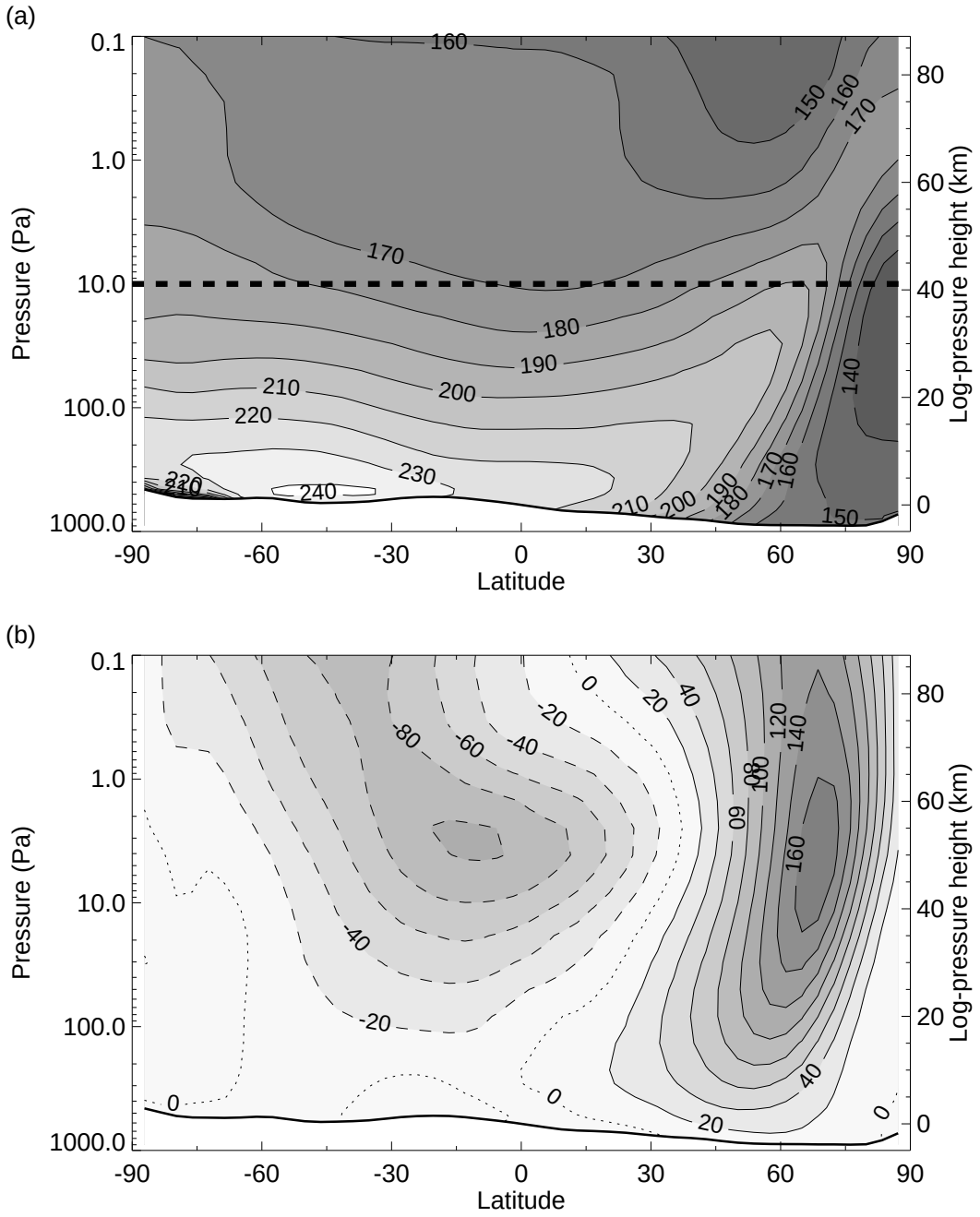

Fig. 8. Lewis et al. Assimilation of atmospheric data during MGS aerobraking

control, indicating that this region is returning to lower dust mixing ratios. Differences in zonal wind are small in the lower atmosphere, Fig. 9(b), with only minor modifications to the northern hemisphere westerly jet tending to increase its horizontal shear as it falls off more rapidly towards the pole in the assimilation. Most notables is the continued westerly flow around 10 km altitude and weaker easterly flow around 60 km altitude above the equator, indicative of the stronger thermal tides in the assimilation.

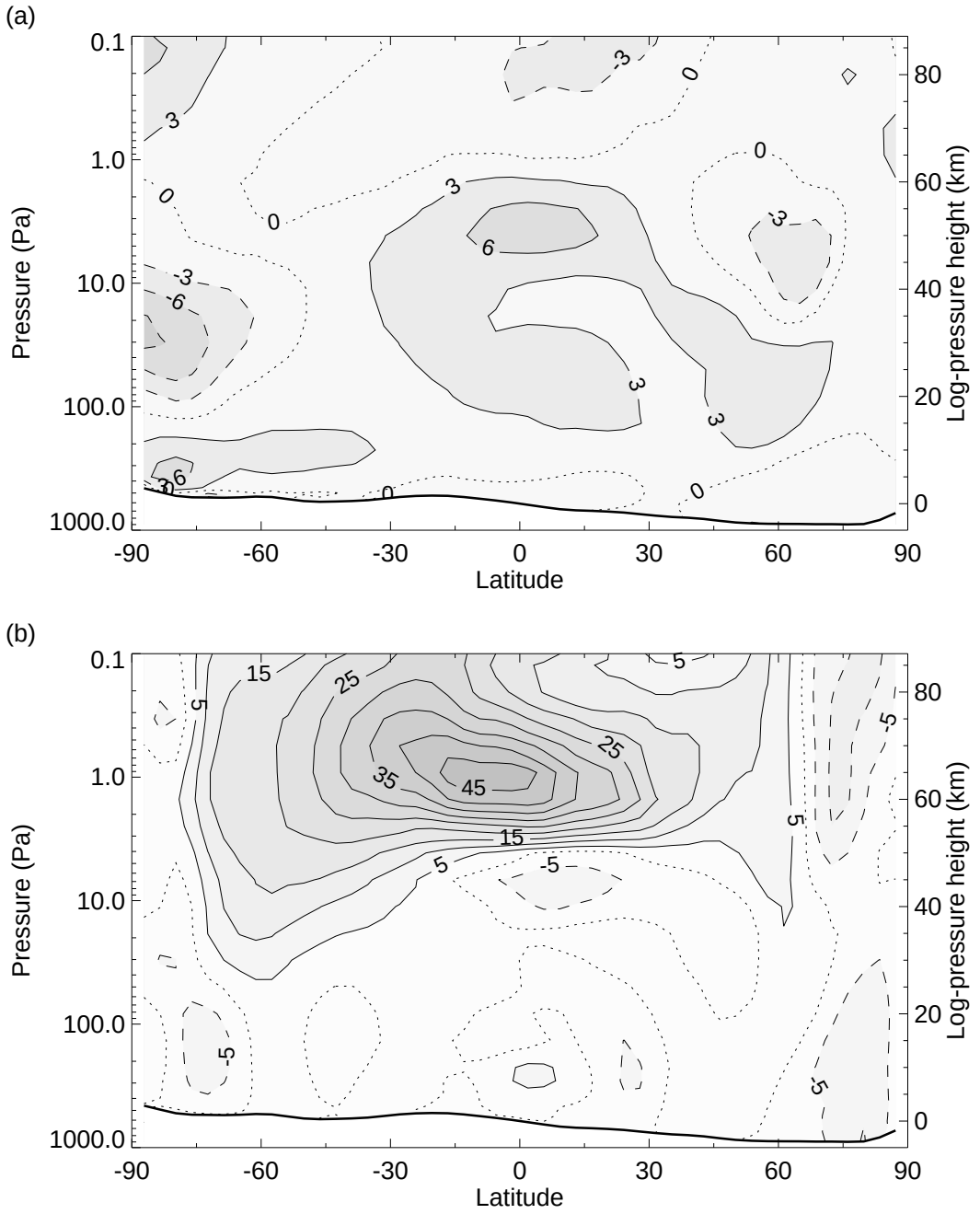

Fig. 9. Lewis et al. Assimilation of atmospheric data during MGS aerobraking

The agreement between zonal-mean temperature and wind fields in the assimilations with those derived directly from the retrievals (Conrath et al., 2000), at least below 40 km, is an indication that the model is responding to the assimilated increments in a reasonable way. Error statistics were also obtained from the assimilation process. The mean and root-mean-square (RMS) difference between the model predictions and each retrieved profile, based on the assimilation before that profile was included, were monitored. Figs. 10 and 11 show these statistics for an early assimilation period prior to the Noachis

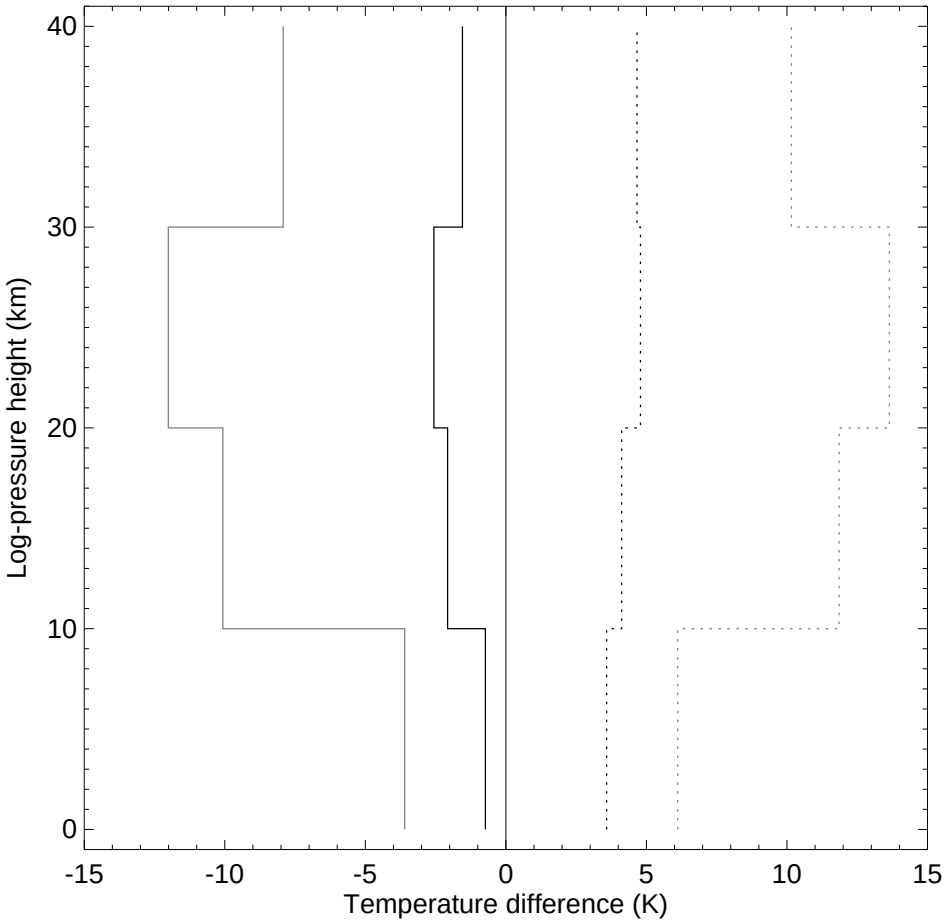

Fig. 10. Lewis et al. Assimilation of atmospheric data during MGS aerobraking

storm, $L_S = 190°$–$215°$, and for a period which includes the Noachis storm, $L_S = 215°$–$240°$. Statistics for a later northern winter period are broadly similar to Fig. 11 and are not shown. In both cases, the comparisons have been made based on the one pressure scale height thickness measure used for the assimilations. The control experiment was sampled and compared with observations at the correct time and place, although no adjustment was made to the model.

Fig. 10 illustrates the mean warm bias, especially between 10 and 30 km, in the control simulation and how this is reduced to around 1–3 K by the assimilation process. Some mean bias remains in the assimilation, with a similar vertical structure to the control experiment. This largely originates from times and locations with few observations, where the model tends to return to its unconstrained thermal state. The RMS differences between the control and observations are even greater and brought down to around 4–5 K by assimi-

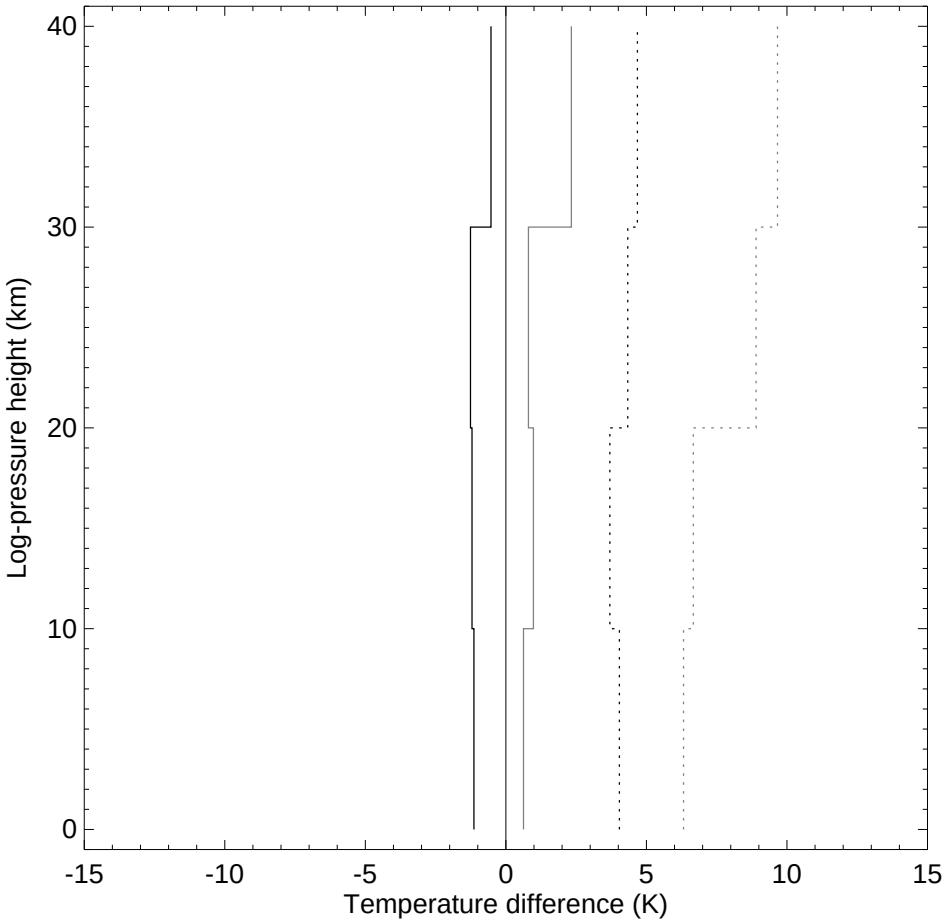

Fig. 11. Lewis et al. Assimilation of atmospheric data during MGS aerobraking

lation.

Fig. 11, from a warmer period with enhanced dust, now indicates that the observations are on average about 1–2 K warmer than the control, whereas the assimilation has a 1 K cool mean bias. This is likely to be because of changes to the dust field and errors in the model radiation schemes which cannot entirely be corrected by assimilation of thermal data. Notably, the RMS error is reduced from about 6–10 K in the control experiment to around 4 K in the assimilation, despite the similar magnitude of the mean biases, an indication that the atmosphere structure is better captured in the assimilation.

The RMS error profile of about 4 K seems to be the limit which can be achieved by this technique over the whole period and is consistent over different time intervals and between assimilations from different initial states. The random errors in the individual temperature retrievals are around 2 K averaged over

the one scale height (or greater) width weighting functions for TES nadir retrievals (Conrath et al., 2000), although they can be higher near the surface. There are also systematic errors (>1 K) in both the retrievals and the model, evidenced by the mean biases in Figs. 10 and 11. More difficult to quantify are errors of representation; the model only represents the large-scale atmospheric features (the grid spacing is 3.75° in longitude and latitude) and interpolates to observation locations, whereas the observations generally have a smaller footprint in the horizontal and thus might resolve smaller-scale features. This would lead to RMS differences even between a perfect model and observation set. The remainder of the 4 K RMS misfit is model error. If a region of the atmosphere has not been observed for some time, the model forecast may increasingly deviate from the true atmospheric temperature evolution in that region. This is likely to be a significant factor in the present case with a long period orbit.

There are some reservations which should be expressed about this simple, global measure of the assimilation error. Firstly, the errors are being measured against the same data set which is being assimilated. This is almost the only option during this period. A more detailed comparison against radio occultation profiles has been conducted for TES assimilations in the spacecraft mapping phase Montabone et al. (2006), though there are relatively few occultations from the aerobraking period which could be used (Hinson et al., 1999). Secondly, the sampling is restricted to the areas where observations are available, which tends to bias away from high northern latitudes, where baroclinic planetary waves would be expected to be growing most strongly at this time of year. It is correspondingly difficult to test conclusively whether baroclinic waves are being assimilated correctly using these data. A more detailed examination of the planetary waves in the assimilations is made in the next section.

6 Transient Waves

Banfield et al. (2000) have already analyzed stationary wave and some tidal information from the MGS TES aerobraking retrievals. Subsequent analyses have discussed stationary and traveling waves during the later MGS mapping phase (Banfield et al., 2003, 2004). An advantage of assimilation lies in its potential ability to diagnose the traveling planetary wave behavior in the atmosphere, something which is difficult to achieve unambiguously by a simple Fourier analysis of the retrievals because of problems associated with aliasing. This is particularly the case when the orbital period is significant compared to typical wave periods, as in the MGS aerobraking phase. Lewis and Read (1995) demonstrated that wave periods and phases could be accurately recovered by assimilation under typical martian conditions, although that study used

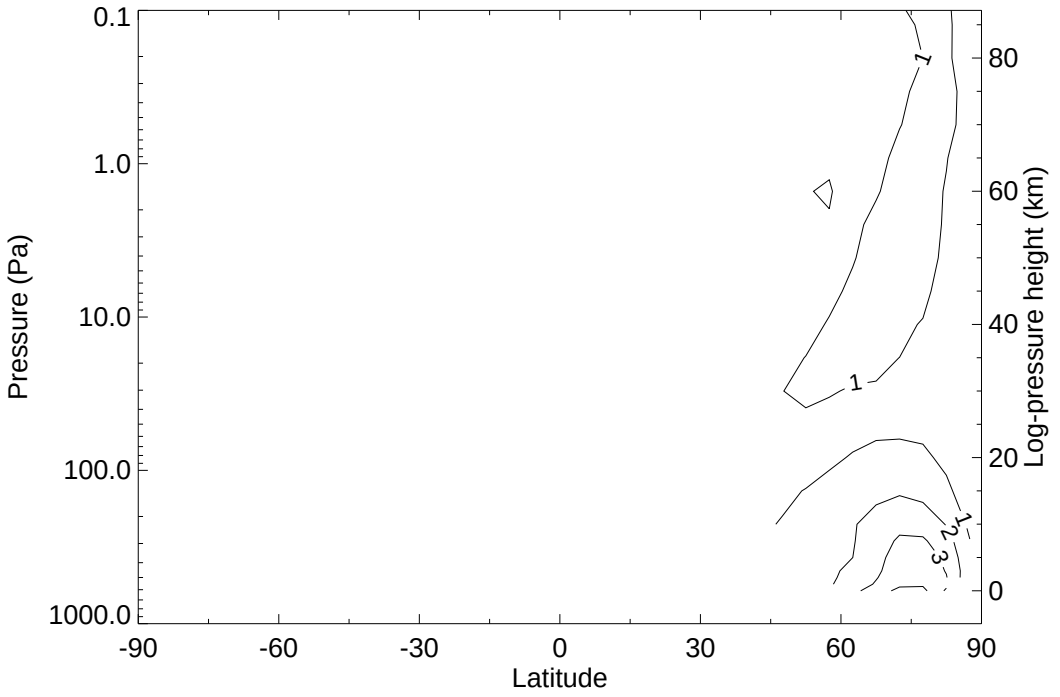

Fig. 12. Lewis et al. Assimilation of atmospheric data during MGS aerobraking

samples made as if from a two-h polar orbit; the longer period, less regular orbital patterns for the present data set are a significantly harder challenge for assimilation.

A straightforward analysis of the transient waves present in the assimilation was made by performing two-dimensional Fourier transforms on the full four-dimensional temperature fields, transformed from the MGCM sigma-level vertical coordinate onto constant pressure surfaces. Figs. 12, 13 and 14 show the amplitude of the largest single mode, as a function of latitude and log-pressure, for the same time intervals as the zonal-mean states shown in Figs. 4–9. In each case the largest amplitude wave mode in the atmospheric temperature was zonal wavenumber one, which can be seen as equivalent to a displacement of the polar vortex. Zonal wavenumber two (not shown) was often significant close to the surface in the northern hemisphere as well, in particular in the first period, $L_S = 190°$–$200°$, when its amplitude very near the surface slightly exceeded that of the wavenumber one mode shown in Fig. 12. The period of the largest wavenumber one component over the three intervals shown was not determined to high precision, since each interval was quite short (17, 13, and 16 sols respectively). It is reasonable to conclude that the dominant mode in the atmospheric temperature field away from the surface is a zonal wavenumber one, propagating eastward, with a period in the region of 5 sols in each case.

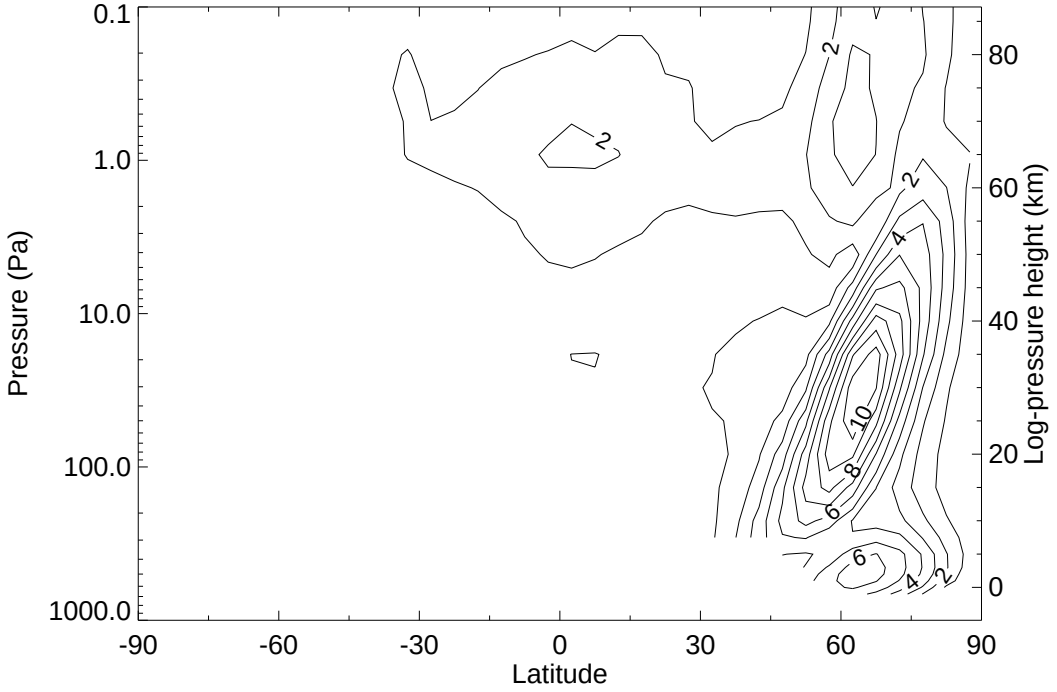

Fig. 13. Lewis et al. Assimilation of atmospheric data during MGS aerobraking

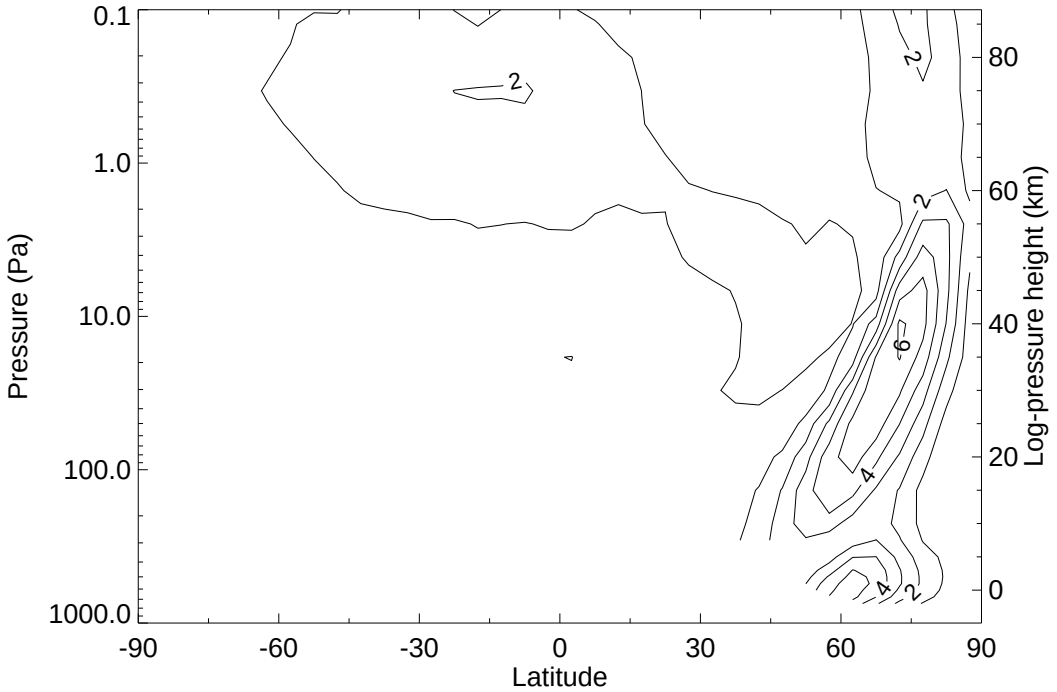

Fig. 14. Lewis et al. Assimilation of atmospheric data during MGS aerobraking

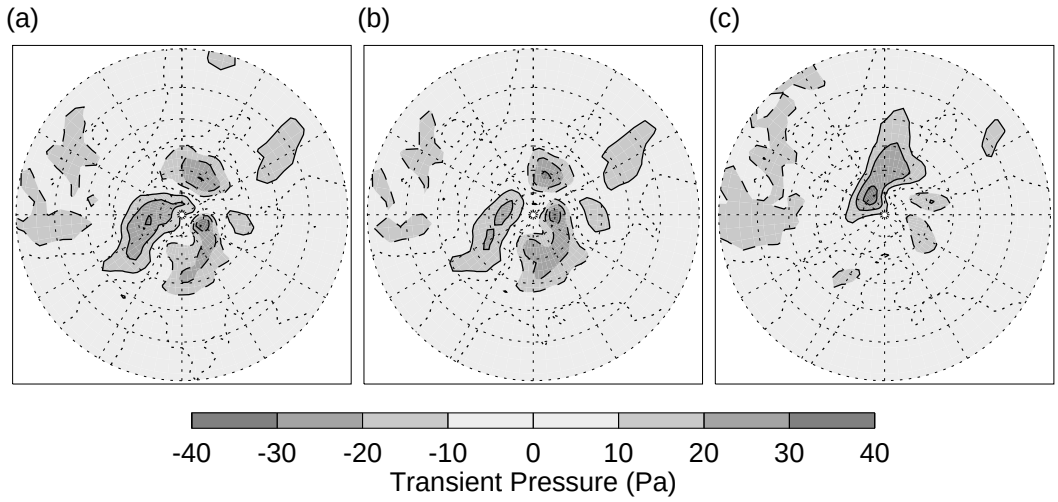

Fig. 15. Lewis et al. Assimilation of atmospheric data during MGS aerobraking

In the autumn, Fig. 12 shows that no significant wave can be detected in the body of the atmosphere; a typical amplitude of around 1–2 K being smaller than the RMS errors in the assimilation misfit. It is notable that there is a stronger wave, reaching nearly 5 K amplitude in both wavenumber one and wavenumber two (not shown), both in a similar region within the lowest atmospheric scale height near the northern, high-latitude surface. The wavenumber two mode is centered slightly further south than the wavenumber one mode, reaching its peak between 55°–75°N and having a typical period of 2.0–2.4 sols. By the time of the Noachis storm, illustrated in Fig. 13, there is evidence of a much stronger atmospheric wave, exceeding 10 K amplitude, centered at 60°N and extending to above 60 km altitude. This is a baroclinic wave, confirmed by a westward phase tilt with height obtained from the Fourier analysis, associated with the strong horizontal temperature gradients in this region, see Fig. 6a. A secondary peak remains near the surface and has grown slightly since Fig. 12. As winter solstice approaches (Fig. 14), and the Noachis storm dies away, the middle atmosphere mode in the northern hemisphere is still prominent, but has a reduced magnitude, although the component of the mode trapped near the surface seems to be of roughly the same amplitude as before at 5–6 K.

Fourier analysis of the assimilated record also showed some wave activity at higher zonal wavenumbers, three and four, and in the southern hemisphere mid-latitudes. The amplitude of these waves was, however, not signficant compared to the typical RMS errors.

In order to further test whether the assimilations were capturing the actual transient waves, rather than simply modifying the MGCM thermal state to produce transient modes of different strengths and locations but essentially uncorrelated between different assimilations, a small ensemble of assimilations

was conducted from a set of different, but equally plausible, initial conditions. One example is shown in Fig. 15. This shows the transient surface pressure (a 20 sol, time-centered running-mean is removed to emphasize transient behavior over topographic effects) from the northern hemisphere of two assimilations and a control integration at $L_S = 200°$, about 17 sols into the assimilation period. The transient modes can be seen as strong zonal wavenumber one and two disturbances near the center of the plot, with surface pressure variations nearer the equator resulting from the atmospheric thermal tides. In this case, both assimilations were conducted identically, but the atmospheric initial states used for each assimilation at $L_S = 189.7°$ were taken from two successive records made exactly one sol apart (both at midnight on the prime meridian) in the control model simulation. The control experiment was continued from the same state as the first assimilation at sol zero; the second assimilation was initialized at sol zero using the control model state from sol one. Since the model at that point was dominated by a surface pressure wavenumber two disturbance, with a period close to two sols, this placed the waves in the initial states for the two assimilations in anti-phase with each other.

It is immediately striking that the high and low pressure systems correlate at the time shown in Fig. 15 between both assimilations, and are somewhat stronger than in the control experiment. This suggests that not only are the wave properties in general being modified by assimilation, but the wave phases are being obtained consistently. A small ensemble of nine assimilations seems to confirm this, at this point in the assimilation. The observation that it takes around 10–20 sols to bring waves in different assimilations into phase with each other during the MGS aerobraking phase is consistent with earlier experience from trial experiments with this scheme (Lewis et al., 1997) that it requires of order 10 orbits of data for the assimilation to converge from arbitrary initial conditions. The corresponding convergence period may be reduced closer to one sol in the MGS mapping phase with 2-h orbits.

It should be noted that the assimilations are exhibiting consistent behavior in their surface pressure fields, whereas the data being assimilated are atmospheric temperature often with reduced coverage close to the surface. It is not obvious that it would be easy for perturbations to the air temperatures to affect the surface pressure. Rather, the terrestrial meteorological experience would suggest that surface pressure observations are crucial and tend to drive behavior in the atmosphere above (Lorenc et al., 1991), so this example of assimilation being able to modify the surface pressure field in the absence of direct observations is noteworthy, as previously demonstrated by Kass (1999).

Fig. 16a shows surface pressure from a single assimilation and the control experiment at one northern high latitude location; 62.5°N, 0°E, was chosen to avoid much signal from the thermal tides and to be near the region where the transient waves have large amplitude. Means and seasonal trends have been

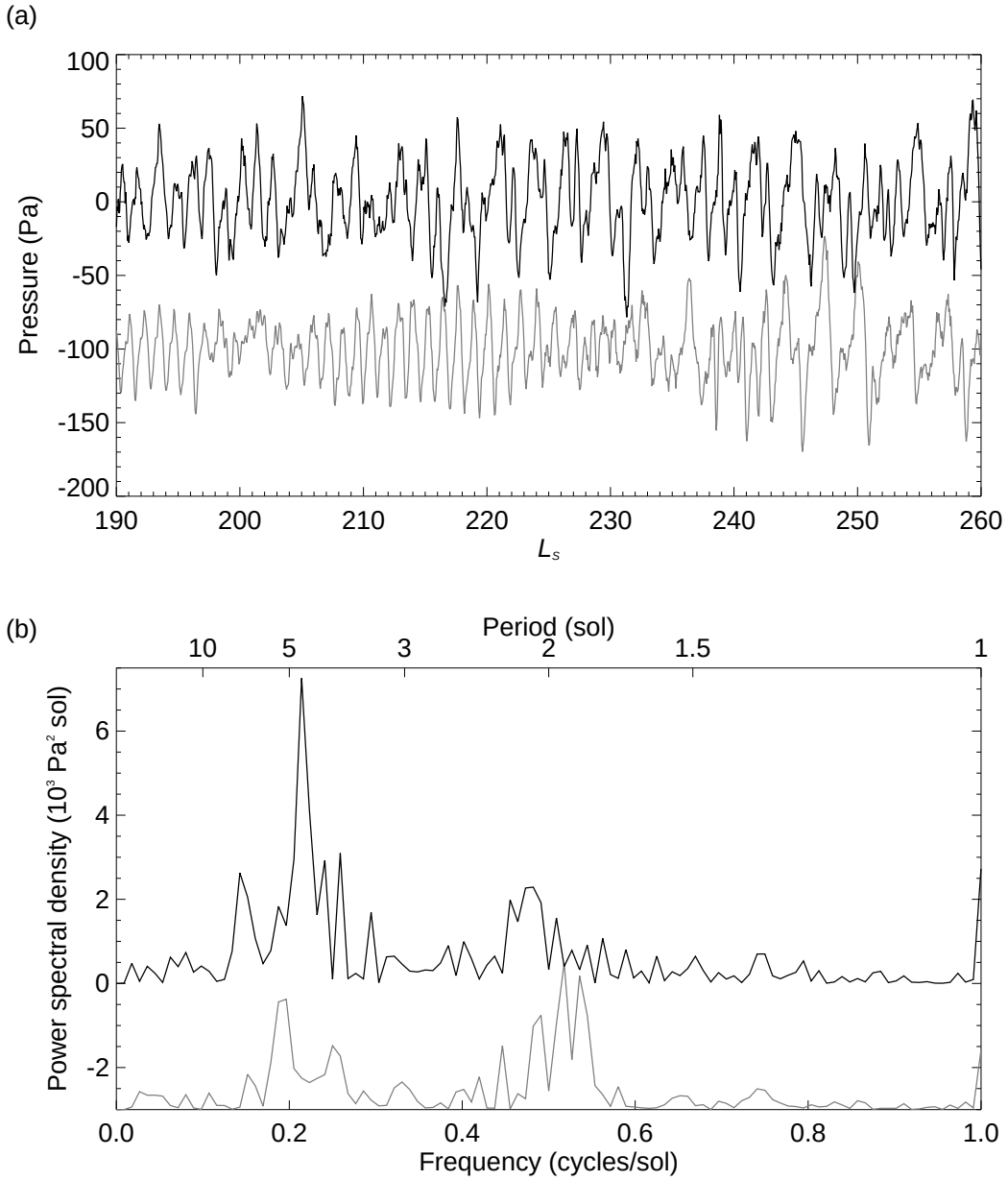

Fig. 16. Lewis et al. Assimilation of atmospheric data during MGS aerobraking

removed by subtracting a best-fit fourth order polynomial. Both experiments shown were begun from identical initial states. Despite some initial similarities between the pressure curves, coherence is rapidly lost over a few sols; the surface pressure curve for the control experiment is in anti-phase with the assimilation after only four wave periods. Only one assimilation has been shown here for clarity, but others show a similar pattern in surface pressure at this site, with the development of larger transient waves with a period of close to 5 sols early in the record, compared to the more persistent 2 sol wave in the control experiment.

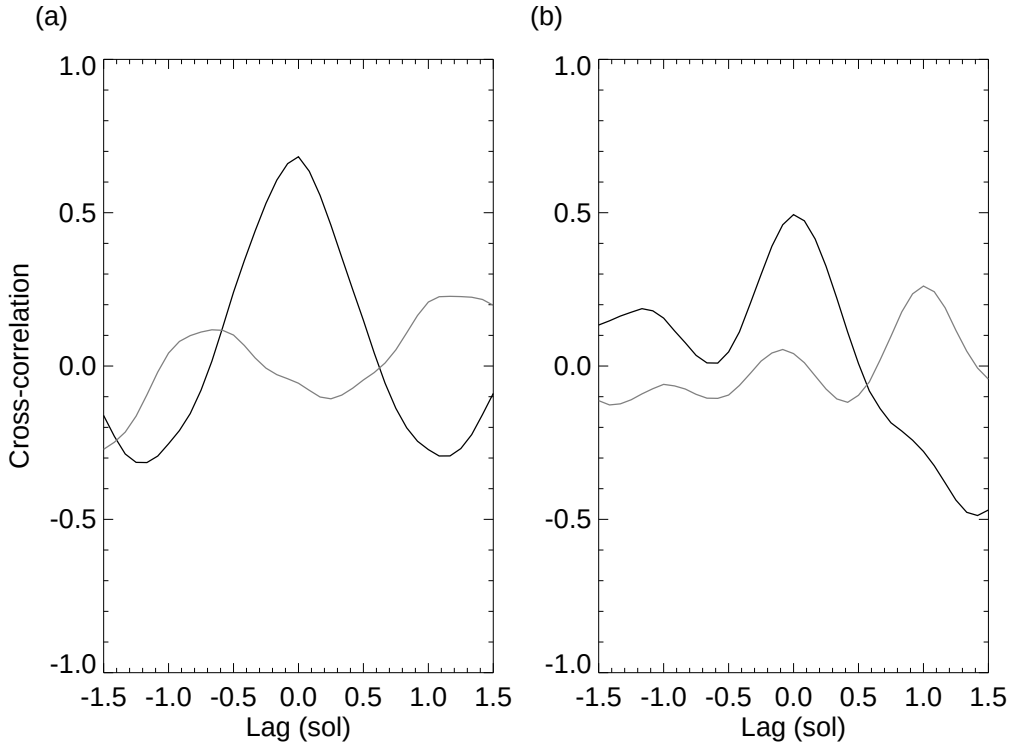

Fig. 17. Lewis et al. Assimilation of atmospheric data during MGS aerobraking

The power spectral density of both curves is given in Fig. 16(b) and shows significant narrow peaks in the assimilation surface pressure spectrum. The assimilation shows a particularly strong peak close to a period of 5 sols, with some evidence of longer periods around 6–7 sols, corresponding to a primarily zonal wavenumber one flow, which appears at a later time in the record and much less clearly in the control experiment. While the control experiment has a broad peak around a period of 2 sols, a zonal wavenumber two state which dominates until around $L_S = 245°$, the assimilation shows a narrower peak at a slightly longer period of around 2.3 sols, associated with zonal wavenumber two flow in the early part of the record, until $L_S = 210°$. The assimilation also shows evidence of a stronger diurnal (and semi-diurnal, not shown) cycle as a result of the increased dust loading in the later part of the assimilation period. These main differences in spectrum are consistent over a range of assimilations with varying initial conditions; only one case is shown here for clarity. It seems reasonable to identify the two modes observed in the surface pressure fields with the components of the atmospheric temperature analysis which are seen trapped near the surface, a zonal wavenumber one mode with a period of around 5 sols in Figs. 12–14 and a zonal wavenumber two mode also detected with a period around 2.0-2.4 sols.

In order to provide a test of the robustness of the transient wave results at the surface, a comparison of the surface pressure at the 62.5°N, 0°E point was made with a second member of the ensemble which had transient waves in anti-

phase at $L_S = 189.7°$, as used earlier in Fig. 15. The surface pressure from this second assimilation throughout the assimilation period was cross-correlated with that from the first assimilation, shown in Fig. 16, and the results are shown in Fig. 17 for two 30 sol periods early and later in the experiment, (a) $L_S = 192°$–$210°$ and (b) $L_S = 230°$–$250°$. Cross-correlation between the curves was calculated over a range of possible time-lags between the curves; only lags between ± 1.5 sols are shown, there were no significant correlations at longer lags. In Fig. 17a there is a clear positive correlation between the assimilations when compared at zero time lag; the surface pressure at this point in the two assimilations varies in a very similar way at the same time. It is also notable that the cross-correlation is almost symmetric with varying lag between the curves and that there is significant anti-correlation between the curves at lags of $\approx \pm 1.1$–1.3 sols, indicating the presence of a wave with a period broadly in the region of 2.2–2.6 sols, as observed in Fig. 16(b).

The two assimilations continue to almost "shadow" each other until after $L_S = 210°$. This in contrast to the control experiment. A similar cross-correlation is shown in gray in Fig. 17a between one assimilation and the control, both as shown in Fig. 16. This shows no evidence of correlation between the surface pressure in the assimilation and control over this period at any relative lag, despite the fact that this assimilation experiment had identical initial conditions to the control. The same is true for comparisons between the control and other assimilations with differing initial conditions.

Around $L_S = 215°$ coherence between the waves in the two assimilations considered here is lost. This coincides with two events. Firstly, both assimilations are in the process of transition from primarily a shorter period (2.3 sol) zonal wavenumber two flow to a flow dominated by a longer period (5 sol) zonal wavenumber one wave. Secondly, and probably crucially, this is the point at which there is no data to assimilate for several sols, see Fig. 3. The loss of coherence emphasizes that the assimilation of temperature data is vital for the surface pressure signal to remain in phase between the two runs. Both assimilations produce a stronger wave throughout the later Noachis storm period, with a similar period, but they are not coherent in phase. This is hardly surprising, given that wave coherence was lost before the storm and that during it there are fewer temperature profiles, especially at northern high latitudes. After the Noachis storm, the correlation between the surface pressure fields grows again and there is evidence of positive cross-correlation between both assimilations over $L_S = 230°$–$250°$ at zero time lag in Fig. 17(b). This is despite the clear difficulties in regaining wave coherence in this challenging case with a relatively long-period orbit and short atmospheric radiative timescales in a dusty atmosphere. The correlation between the assimilations is not as strong in Fig. 17(b) as in the earlier period in Fig. 17a, but it should be noted from Fig. 3 that this second period includes a further interruption in data, and a second loss of wave coherence, around $L_S = 242°$.

7 The Noachis Dust Storm

The Noachis dust storm period is a particularly stern test for the assimilation scheme and is worth some specific consideration. Given sufficient temperature data, trial experiments using non-identical twin models (Lewis et al., 1997) have shown that assimilation can remain accurate up to differences in visible optical depths of around $\tau = 1$ between the models. However, there are fewer temperature profiles available during the aerobraking period, and furthermore the Noachis storm dust opacity reaches optical depths greater than $\tau = 2$ in the visible (Smith et al., 2000) and is non-uniformly distributed. Zhang et al. (2001) also appeared to find difficulties in real case assimilations with relatively minor differences in optical depth. For these reasons, the assimilations shown here were attempted both with temperature data alone (as in Lewis et al., 1997; Zhang et al., 2001) and with the dust field updated by the assimilation scheme as described in Sec. 4. Even this second option is not entirely satisfactory, both because of the problems with the dust observations outlined earlier and because observations were only available over a restricted range of longitudes and latitudes at any one time and hence the dust field in the model could not evolve in a realistic way simultaneously at all locations. It is possible in principle for the MGCM to transport dust, and to predict deposition and lifting by wind stress or dust devils (Newman et al., 2002a,b), but these schemes are difficult to calibrate and were turned off here to avoid the introduction of too many complications in the first instance. Nonetheless, the evidence shown in this section seems to indicate that assimilation of dust information may have a very beneficial impact on the assimilation when the dust opacity becomes high.

Fig. 18 illustrates the changing distribution of total dust opacity output from the model assimilation at 4 sol intervals, one just prior to the onset of the Noachis storm and the others following its development. The final plot shows the atmosphere 24 sols after the onset of the main storm. The dust field is smoothed by the spreading effects of the horizontal correlation function (see Eq. 2) and some parts of the atmosphere have few dust observations influencing them during this time. Fig. 18 still shows clearly the development of a storm with optical depths exceeding 2.5 in the visible in the Noachis region at 30°S, the movement of the dust poleward and eastward as the storm decays, and the development of a subsequent, smaller dust peak around 60°S, as described by Smith et al. (2000). It is noteworthy that, even in the first frame, 4 sols before the main Noachis storm begins, the dust distribution is far from uniform with opacities rising locally to $\tau > 0.8$ compared to a background level of $\tau \leq 0.4$.

The development of the Noachis storm during the assimilation period is effectively shown in Fig. 19 in terms of zonal mean temperatures on the 30 Pa surface at 30°N and 30°S. A control experiment is shown, in which no storm

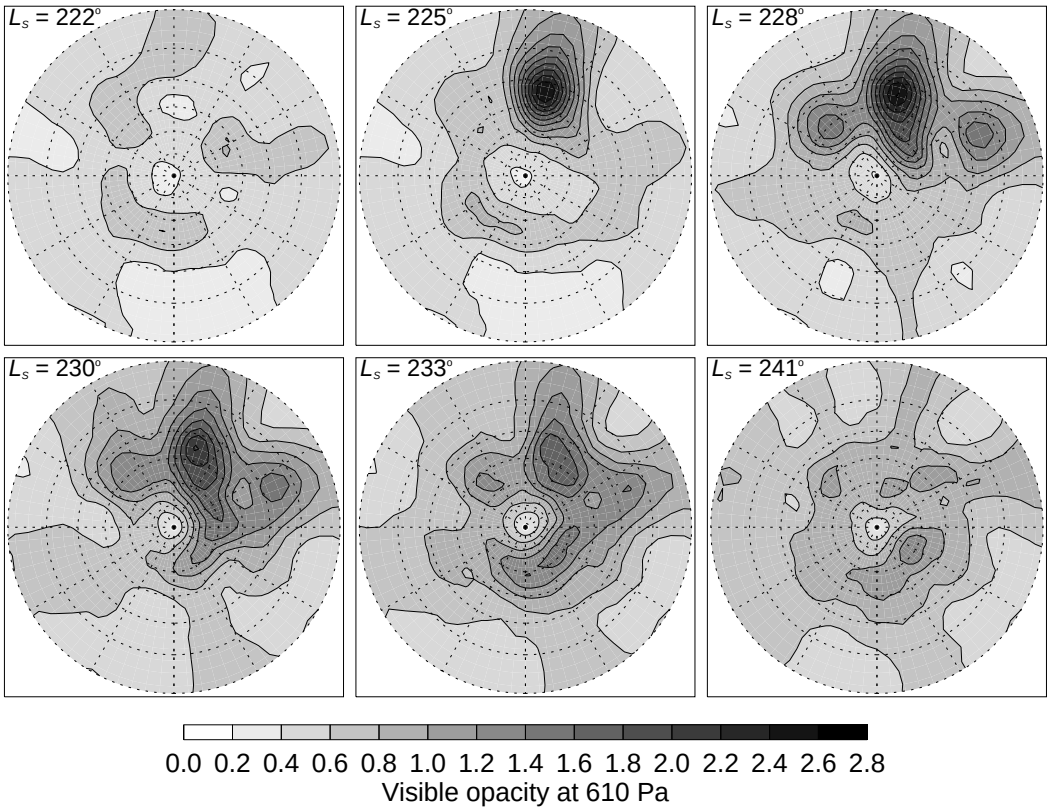

Fig. 18. Lewis et al. Assimilation of atmospheric data during MGS aerobraking

takes place and the curves progress smoothly through the seasonal temperature cycle. The small wiggles on the curve are caused by zonal asymmetries in the diurnal thermal tide, associated with surface thermal properties and topography; were their amplitudes perfectly uniform in longitude, the curve should be smooth since it is a true zonal mean. Two assimilations are shown, as in Fig. 16, one with assimilation of both temperature profiles and dust and one with a temperature assimilation alone. Both start from the same initial conditions as the control experiment at $L_S = 189.7°$, and both rapidly cool at this height compared to the control. Until $L_S = 225°$, the two assimilations shadow each other. Even though there are local dust variations of over 50 per cent, there is sufficient temperature information to provide a consistent assimilation. This includes the period from $L_S = 220°$–$225°$, when the atmosphere can be seen to warm prior to the main Noachis storm. One feature of note in this period is the apparent warming beginning around $L_S = 215°$ which seems to last for several sols. This is purely the effect of the lack of any observations around this time, as indicated earlier. Without temperature observations, the assimilations tend to return to the same temperatures at this height as predicted by the control. Although the horizontal dust distribution has been updated in one assimilation, the vertical distribution is not changed and it might be errors in this, perhaps in combination with errors in other model schemes, which lead to a prediction of temperature which is up to 5 K

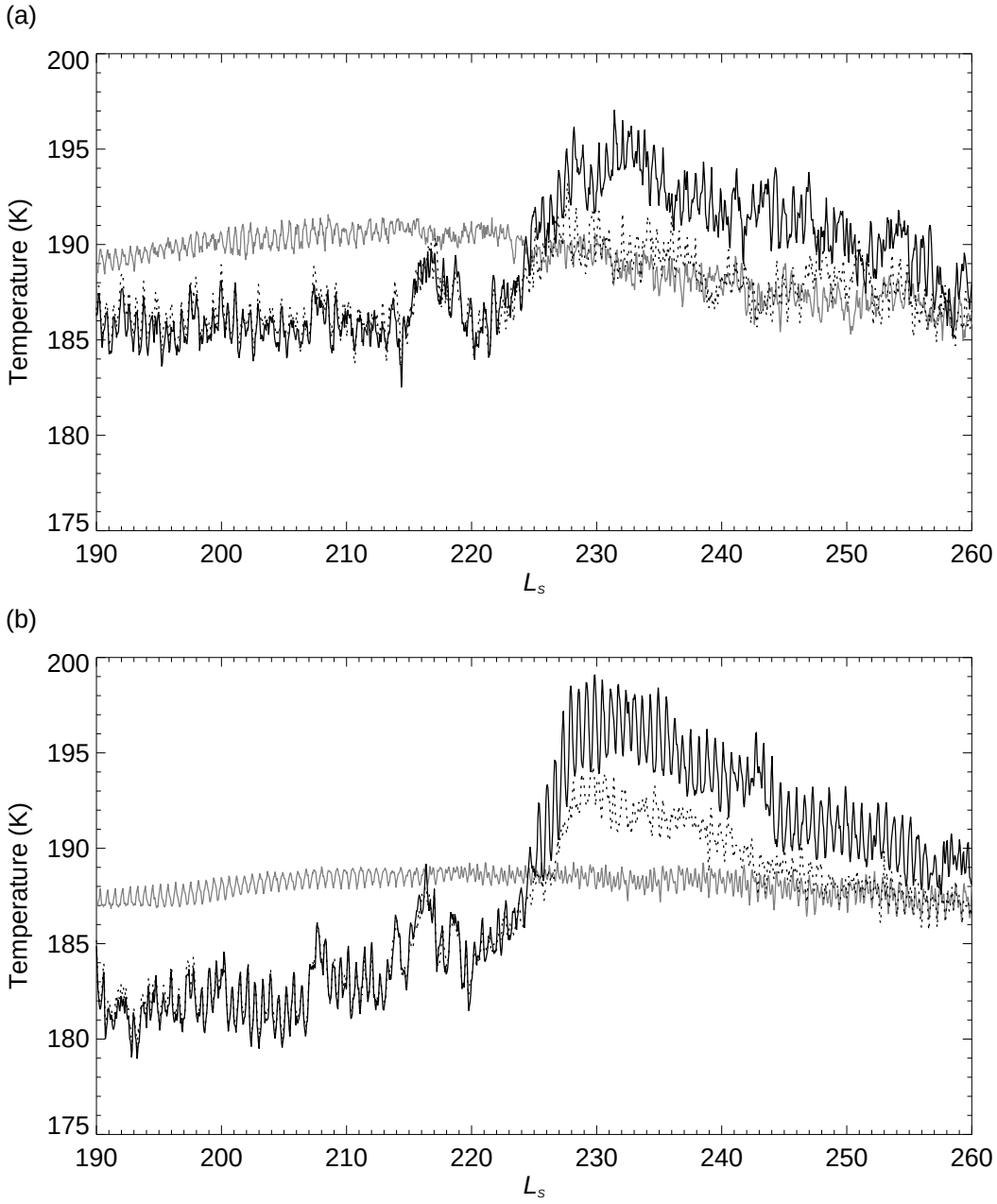

Fig. 19. Lewis et al. Assimilation of atmospheric data during MGS aerobraking

too warm compared to the assimilations at this height.

The Noachis storm itself is clear as a sudden warming around $L_S = 225°$, especially at 30°S, followed by a gradual cooling over the remaining assimilation period. Here the assimilations do separate, and the assimilation with dust information produces a more dramatic warming, of around 15 K, which is in better agreement with the individual retrievals. For this extreme dust event, therefore, the assimilation with purely temperature data seems to underestimate the degree of warming observed. Nonetheless, it does produce a clear

warming signature, showing the presence of the dust storm. Furthermore the assimilation temperature increments and residuals increase, indicating that the scheme is having to do more work and that the assimilation is fitting the observed temperatures less well. In the assimilation with dust information the assimilation increments do not increase so much because the increased dust loading leads the model to predict higher temperatures and so less temperature correction is needed. Finally, it is notable that the diurnal period oscillation is much stronger in the assimilation experiments, in particular that which makes use of dust information. This is owing to the longitudinally asymmetric dust distribution which leads to an asymmetry in the thermal forcing, with a pulse in the solar heating as the day-side moves over the Noachis region.

Fig. 20 shows the mean meridional circulation from the assimilation including temperature and dust. This illustrates an atmospheric field which can be obtained using assimilation techniques but which is very difficult to measure directly. Averages over two 12 sol periods are shown, (a) just prior to the Noachis dust storm ($L_S = 215°$–$223°$) and (b) starting 3 sols after the end of the first period, a period covering the storm's initial peak ($L_S = 225°$–$233°$). The mean meridional circulation changes rapidly during the full assimilation period, from an equinoctial state with two weaker equatorial cells near $L_S = 190°$ to a growth of the dominant clockwise cross-equatorial circulation, seen in Fig. 20, as northern winter approaches. The two periods compared in Fig. 20 demonstrate the very rapid increase in strength of the martian Hadley circulation with the onset of the Noachis storm. There is a growth of almost 50 per cent in the peak strength of the mean circulation over the course of a few sols. It should also be noted that the meridional circulation becomes much more unsteady after the dust storm initiation, and, at times, the circulation doubles in strength over short periods (≈ 1 sol). The increase in strength of the meridional overturning is reflected in the warming seen very soon after the beginning of the Noachis storm in the northern hemisphere middle atmosphere, a warming which is most intense at longitudes corresponding to the location of the Noachis storm in the southern hemisphere. Conrath et al. (2000) noted that a rapid warming in the northern hemisphere is seen in the TES observations at this time and similar warmings are seen coincident with regional and global dust storms in the subsequent TES mapping phase data (Smith et al., 2001) and in earlier Viking IRTM observations (Martin and Kieffer, 1979; Jakosky and Martin, 1987). The northern hemisphere warming is most pronounced in the assimilation with dust information, as is the growth in the mean meridional circulation seen in Fig. 20(b). In the case of temperature assimilation only (not shown), the meridional circulation does strengthen by a few per cent around the onset of the Noachis storm, but remains closer to Fig. 20a throughout. The pronounced circulation growth with the onset of the Noachis storm is only seen when dust information is included in the assimilation. This again highlights the value of combining different atmospheric measurements, especially in this period when there is not continuous, global

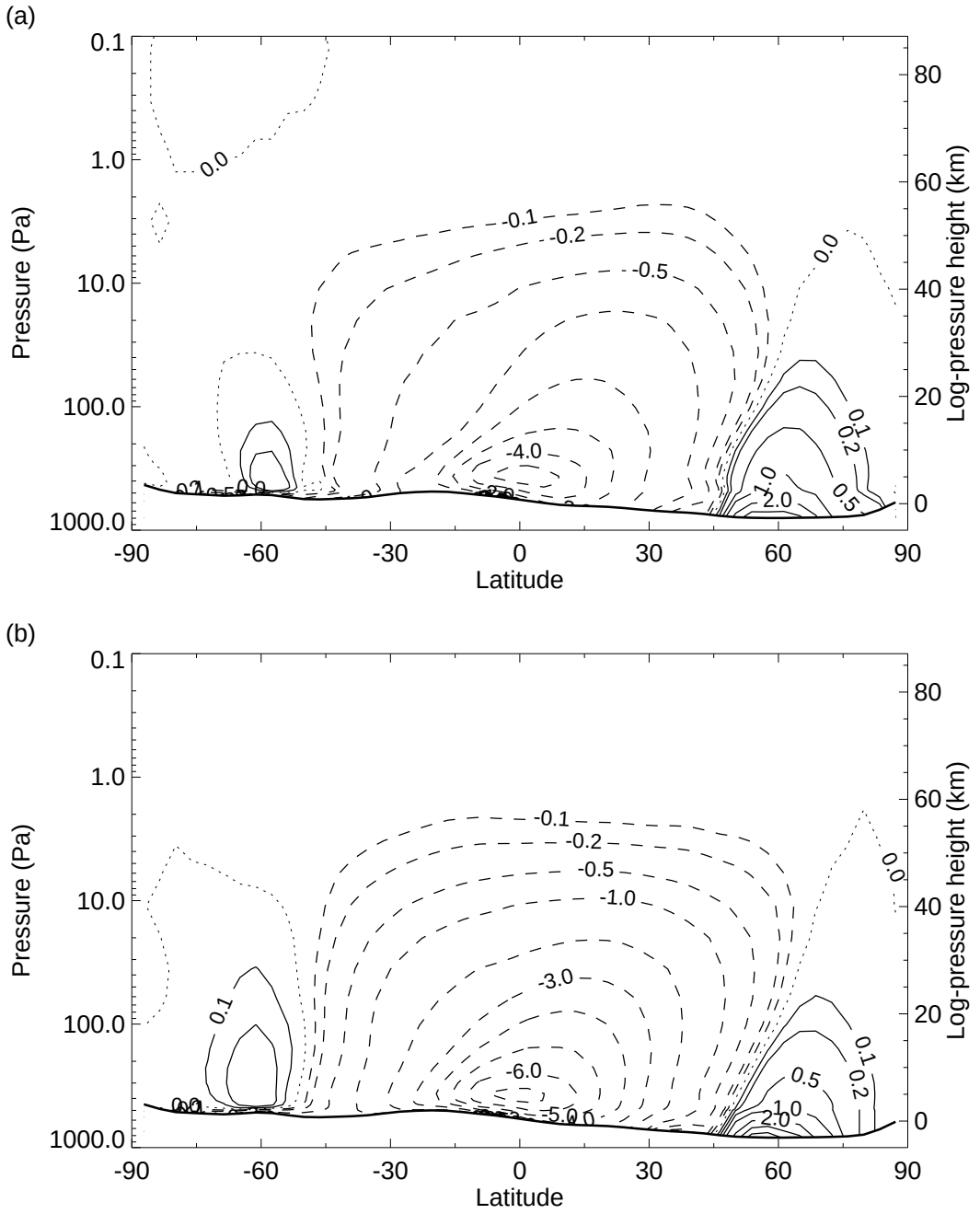

Fig. 20. Lewis et al. Assimilation of atmospheric data during MGS aerobraking

temperature coverage and in which the circulation is changing rapidly.

8 Conclusions

The analysis correction data assimilation scheme, as applied to the MGCM here, appears to exhibit a considerable degree of success in assimilating TES observations from the MGS aerobraking phase. This is despite the problems inherent in the irregular and intermittent coverage pattern and the limitation to nadir soundings of low effective vertical resolution. The analysis scheme has some parameters which must be tuned empirically and is not optimal statistically, but is computationally efficient and robust with a real data set and a realistic MGCM. Comparable assimilations in future, for example with a more complicated four-dimensional variational scheme, which should, at least in principle, be able to extract more information from the observational data set, would provide useful context and a further test of the validity of the results.

The assimilation procedure adopted here is already able to demonstrate some of the advantages of assimilation: the derivation of a self-consistent set of all atmospheric variables at all locations and times from a more limited range of observations; the ability to correct a model which is making some incorrect assumptions given sufficient thermal data, e.g. the indication of errors in the dust distribution; and the provision of a four-dimensional data set in which synoptic-scale and transient features can be diagnosed without ambiguity.

Results from the Noachis storm period demonstrate the value of adding information from dust retrievals, although even with temperature data alone the assimilation is able to detect the presence of the storm and to indicate that the model heating rates are substantially in error, i.e. that the dust field is incorrect. Further studies with the present assimilation procedure will ideally include the assimilation of dust in an MGCM which has a complete operational dust cycle, and an attempt to assimilate water ice and vapor information would also be of interest. The scheme will also be extended in future to assimilate radiances directly.

The results presented in this study are not only of interest in their own right, but indicate that it is worthwhile applying the same assimilation procedure to the full scientific mapping phase data set, an effort which has already commenced, to study specific features of the martian atmospheric circulation and climate (Lewis and Barker, 2005; Montabone et al., 2005, 2006).

Acknowledgements

SRL and PLR are grateful for support for this work from the UK Particle Physics and Astronomy Research Council. BJC acknowledges support from the NASA Mars Data Analysis Program. We thank Claire Newman for helpful comments on an early version of the manuscript.

References

Banfield, D., Conrath, B. J., Gierasch, P. J., Wilson, R. J., Smith, M. D., 2004. Traveling waves in the martian atmosphere from MGS TES nadir data. Icarus 170, 365–403.

Banfield, D., Conrath, B. J., Pearl, J. C., Smith, M. D., Christensen, P. R., 2000. Thermal tides and stationary waves on Mars as revealed by Mars Global Surveyor Thermal Emission Spectrometer. J. Geophys. Res. 105, 9521–9537.

Banfield, D., Conrath, B. J., Smith, M. D., Christensen, P. R., Wilson, R. J., 2003. Forced waves in the martian atmosphere from MGS TES nadir data. Icarus 161, 319–345.

Banfield, D., Ingersoll, A., Keppenne, C., 1995. A steady-state Kalman filter for assimilating data from a single polar-orbiting satellite. J. Atmos. Sci. 52, 737–753.

Clancy, R. T., Lee, S. W., Gladstone, G. R., McMillan, W. W., Rousch, T., 1995. A new model for Mars atmospheric dust based upon analysis of ultraviolet through infrared observations from Mariner 9, Viking, and Phobos. J. Geophys. Res. 100 (E3), 5251–5263.

Conrath, B. J., 1975. Thermal structure of the martian atmosphere during the dissipation of the dust storm of 1971. Icarus 24, 36–46.

Conrath, B. J., Pearl, J. C., Smith, M. D., Maguire, W. C., Dason, S., Kaelberer, M. S., Christensen, P. R., 2000. Mars Global Surveyor Thermal Emission Spectrometer (TES) observations: Atmospheric temperatures during aerobraking and science phasing. J. Geophys. Res. 105 (E4), 9509–9519.

Daley, R., 1991. Atmospheric Data Analysis. Cambridge University Press, Cambridge, UK.

Davies, H. C., Turner, R. E., 1977. Updating prediction models by dynamical relaxation: An examination of the technique. Quart. J. R. Meteor. Soc. 103, 225–245.

Forget, F., Hourdin, F., Fournier, R., Hourdin, C., Talagrand, O., Collins, M., Lewis, S. R., Read, P. L., Huot, J.-P., 1999. Improved general circulation models of the martian atmosphere from the surface to above 80 km. J. Geophys. Res. 104 (E10), 24155–24176.

Haberle, R. M., Jakosky, B. M., 1991. Atmospheric effects on the remote determination of the thermal inertia of Mars. Icarus 90, 187–204.

Haberle, R. M., Pollack, J. B., Barnes, J. R., Zurek, R. W., Leovy, C. B., Murphy, J. R., Lee, H., Schaeffer, J., 1993. Mars atmospheric dynamics as simulated by the NASA/Ames general circulation model, 1, The zonal-mean circulation. J. Geophys. Res. 98, 3093–3123.

Hayashi, J. N., Jakosky, B. M., Haberle, R. M., 1995. Atmospheric effects on the mapping of martian thermal inertia and thermally derived albedo. J. Geophys. Res. 100, 5277–5284.

Hinson, D. P., Simpson, R. A., Twicken, J. D., Tyler, G. L., Flasar, F. M., 1999. Initial results from radio occultation measurements with Mars Global Surveyor. J. Geophys. Res. 104, 26997–27012.

Houben, H., 1999. Assimilation of Mars Global Surveyor meteorological data. Adv. Space Res. 23 (11), 1899–1902.

Jakosky, B. M., Martin, T. Z., 1987. Mars: North-polar atmospheric warming during dust storms. Icarus 72, 528–534.

Kass, D. M., 1999. Change in the martian atmosphere. Ph.D. thesis, Planetary Science, California Institute of Technology, Pasadena.

Lewis, S. R., Barker, P., 2005. Atmospheric tides in a Mars general circulation model with assimilation of Mars Global Surveyor data. Adv. Space Res. 36 (11), 2162–2168.

Lewis, S. R., Collins, M., Read, P. L., 1996. Martian atmospheric data assimilation with a simplified general circulation model: Orbiter and lander networks. Plan. Space Sci. 44, 1395–1409.

Lewis, S. R., Collins, M., Read, P. L., 1997. Data assimilation with a martian atmospheric GCM: An example using thermal data. Adv. Space Res. 19(8), 1267–1270.

Lewis, S. R., Read, P. L., 1995. An operational data assimilation scheme for the martian atmosphere. Adv. Space Res. 16(6), 9–13.

Lewis, S. R., Read, P. L., 2003. Equatorial jets in the dusty martian atmosphere. J. Geophys. Res. 108 (E4), 5034, doi:10.1029/2002JE001933.

Lorenc, A. C., Bell, R. S., Macpherson, B., 1991. The Meteorological Office analysis correction data assimilation scheme. Quart. J. R. Meteor. Soc. 117, 59–89.

Lyne, W. H., 1979. Data assimilation by repeated correction of model fields. Tech. Rep. Met. O. 11 Tech. Note No. 130, U.K. Meteorological Office.

Martin, T. Z., 1986. Thermal infrared opacity of the Mars atmosphere. Icarus 66, 2–21.

Martin, T. Z., Kieffer, H. H., 1979. Thermal infrared properties of the martian atmosphere, 2, the 15 μm band measurements. J. Geophys. Res. 84, 2843–2852.

Mellon, M. T., Jakosky, B. M., Kieffer, H. H., Christensen, P. R., 2000. High resolution thermal inertia mapping from the Mars Global Surveyor Thermal Emission Spectrometer. Icarus 148, 437–455.

Montabone, L., Lewis, S. R., Read, P. L., 2005. Interannual variability of

martian dust storms in assimilation of several years of Mars Global Surveyor observations. Adv. Space Res. 36 (11), 2146–2155.

Montabone, L., Lewis, S. R., Read, P. L., Hinson, D. P., 2006. Validation of martian meteorological data assimilation for MGS/TES using radio occultation measurements. Icarus 185 (1), 113–132.

Newman, C. E., Lewis, S. R., Read, P. L., Forget, F., 2002a. Modeling the martian dust cycle, 1. Representations of dust transport processes. J. Geophys. Res. 107 (E12), doi:10.1029/2002JE001910.

Newman, C. E., Lewis, S. R., Read, P. L., Forget, F., 2002b. Modeling the martian dust cycle, 2. multiannual radiatively active dust transport simulations. J. Geophys. Res. 107 (E12), doi:10.1029/2002JE001920.

Paige, D. A., Bachman, J. E., Keegan, K. D., 1994. Thermal and albedo mapping of the polar regions of Mars using Viking thermal mapper observations, 1. North polar region. J. Geophys. Res. 99, 25959–25991.

Paige, D. A., Keegan, K. D., 1994. Thermal and albedo mapping of the polar regions of Mars using Viking thermal mapper observations, 2. South polar region. J. Geophys. Res. 99, 25993–26013.

Palluconi, F. D., Kieffer, H. H., 1981. Thermal inertia mapping of Mars from 60°S to 60°N. Icarus 45, 415–426.

Smith, D. E., Zuber, M. T., Frey, H. V., Garvin, J. B., Head, J. W., Muhleman, D. O., Pettengill, G. H., Phillips, R. J., Solomon, S. C., Zwally, H. J., Banerdt, W. B., Duxbury, T. C., 1998. Topography of the northern hemisphere of Mars from the Mars Orbiter Laser Altimeter. Science 279, 1686–1692.

Smith, M. D., Pearl, J. C., Conrath, B. J., Christensen, P. R., 2000. Mars Global Surveyor Thermal Emission Spectrometer (TES) observations of dust opacity during aerobraking and science phasing. J. Geophys. Res. 105 (E4), 9539–9552.

Smith, M. D., Pearl, J. C., Conrath, B. J., Christensen, P. R., 2001. Thermal Emission Spectrometer results: Mars atmospheric thermal structure and aerosol distribution. J. Geophys. Res. 106 (E10), 23929–23945.

Wilson, R. J., 1997. A general circulation model simulation of the martian polar warming. Geophys. Res. Lett. 24, 123–126.

Zhang, K. Q., Ingersoll, A. P., Kass, D. M., Pearl, J. C., Smith, M. D., Conrath, B. J., Haberle, R. M., 2001. Assimilation of Mars Global Surveyor atmospheric temperature data into a general circulation model. J. Geophys. Res. 106 (E12), 32863–32877.